Optics & Laser Technology 173 (2024) 110534

Contents lists available at ScienceDirect

Optics and Laser Technology

journal homepage: www.elsevier.com/locate/optlastec

Full length article

Effect of post-weld heat treatment on the microstructure, phase composition and mechanical properties of dissimilar Al-Mg-Li/Al-Cu-Li laser welded joints

Alexander Malikov [a,*], Igor Vitoshkin [a], Artem Filippov [a], Evgeniy Karpov [b], Konstantin Kuper [c]

[a] Khristianovich Institute of Theoretical and Applied Mechanics Siberian Branch Russian Academy of Sciences, Institutskaya Str. 4/1, Novosibirsk 630090, Russia
[b] Lavrentyev Institute of Hydrodynamics Siberian Branch Russian Academy of Sciences, Lavrentyev Ave. 15, Novosibirsk 630090, Russia
[c] Budker Institute of Nuclear Physics of Siberian Branch Russian Academy of Sciences 11, Acad. Lavrentieva Pr., 630090, Russia

ARTICLE INFO

Keywords:
Laser welding
Aluminum–lithium alloy
Microstructure
Phase composition
Mechanical properties
Synchrotron radiation

ABSTRACT

Butt joints of the V-1461 and 1424 heat treated aluminum–lithium alloys of the third generation were welded with a CO_2 laser and studied in detail for the first time. In particular, spatial distributions of the formed phases and their evolution upon post-weld heat treatment (PWHT), determining the mechanical properties of the joints, were investigated. The PWHT included quenching and subsequent artificial aging. The key factors, affecting the metallurgical processes in a weld pool, were the following: 1) the alloying elements and the thermal properties of the alloys, 2) the dynamics of the local non-equilibrium melting, the convective transfer of the molten metal in the weld pool and its subsequent solidification, 3) the cooling rate, and 4) the PWHT procedure. By using synchrotron radiation and scanning electron microscopy, new θ(Al_2Cu), T_1(Al_2CuLi) and S_1(Al_2MgLi) phases were found in the weld metal that were absent in both base metals. This phenomenon reduced the mechanical properties of the joints to the levels, corresponding to about 50 % of the 1424 alloy as the weakest one. Quenching contributed to the formation of the δ′(Al_3Li) strengthening phase in the weld metal. As a result, the ultimate tensile strength increased up to 70 % and elongation up to 95 % of the corresponding levels of the 1424 alloy. Artificial aging made it possible to form the T1(Al_2CuLi) strengthening phase, to increase the content of the δ′(Al_3Li) one, as well as to improve the mechanical properties of the joint. In this case, the ultimate tensile strength was 411 MPa, the yield point was 327 MPa and elongation was 1.7 %. These values were close to those for the 1424 alloy (about 80 %, 89 % and 23 %, respectively).

1. Introduction

When designing advanced aircraft, the characteristics of which must meet severe operating conditions, there is often a need to combine various aerospace alloys. In particular, more than 20 types of aluminum-based grades are used in their manufacturing [1].

Currently, new heat treatable aluminum–lithium alloys of the third generation are widely applied in the aerospace industry [2,3]. They are characterized by reduced lithium contents (<2 wt%), including the following alloying systems: Al-Cu-Li (V-1461, V-1469, 2195, 2196, 2198, etc.); Al-Cu-Mg-Li (1441) and Al-Mg-Li (1424) [1–5]. These alloys are considered as the most promising ones due to their improved functional properties, such as strength, rigidity, ductility, machinability and corrosion resistance. The high mechanical characteristics of these alloys are ensured by a special thermomechanical treatment, as a result of which various phases are formed, including the δ′(Al_3Li), T_1(Al_2CuLi) and θ′(Al_2Cu) hardening ones [1–3,6,7].

Nowadays, many researchers are trying to implement welding of these alloys instead of riveting them in order to improve the process efficiency and to reduce weight of such structures [8]. However, the issue of achieving the required mechanical properties (the ultimate tensile strength, the yield point and elongation) of dissimilar welded joints of the aluminum alloys has not been solved yet. Welding of dissimilar materials is associated with certain difficulties, among which the most significant is the difference in their microstructures, phase compositions and, accordingly, the mechanical properties. The effect of local heating, for example with a laser, also causes such changes in a weld zone. The above-mentioned alloys are characterized by the complexity

* Corresponding author.
E-mail address: smalik@ngs.ru (A. Malikov).

https://doi.org/10.1016/j.optlastec.2023.110534
Received 18 March 2023; Received in revised form 23 October 2023; Accepted 27 December 2023

of their phase transformations upon hot rolling and heat treatment procedures.

Enz et al have studied the effect of changes in the chemical composition on local mechanical properties, such as microhardness and strength, of skin–stringer joints of the 2196 and 2198 aluminum–lithium alloys welded with a CO_2 laser [9]. The obtained results have shown that the chemical composition of the weld metal (WM) is determined by a combination of those for the joined alloys, varying due to both separation and insufficient dilution of some phases in a weld pool.

Liu et al have welded the 2198 and 2060 aluminum–lithium alloys without fillers [10]. The influence of welding parameters on the microstructure evolution, solute segregation, porosity and their relationship with the mechanical properties has been investigated. It has been shown that dissolution of the T_1 and θ' phases, as well as variations in the copper and magnesium contents inside grains and at their boundaries, caused by segregation upon welding, have resulted in a decrease in the strength of the dissimilar joint.

Han et al have fabricated T-shaped dissimilar joints of 2 mm thick plates from the 2060-T8 and 2099-T83 aluminum–lithium alloys using double-sided laser welding with the 4047 filler [11]. The results of the microstructure analysis have shown that segregation in the WM has been characterized by the formation of the T(LiAlSi) and $\theta(Al_2Cu)$ phases with a eutectic at the grain boundaries. Microcracks have been observed at the boundaries between the θ phase and the α-Al matrix, sharply deteriorating corrosion resistance of the joints.

In [12], in-plane shear of the Al-Li-2099/Al-Li-S4 dissimilar L-shaped joints of continuous thin-walled panels, welded with a laser from both sides, has been investigated. The WM has consisted of non-dendritic equiaxed zones, as well as both columnar dendritic and equiaxed dendritic ones. In tensile testing, a crack has initiated in the WM and propagated into the base metal (BM).

Chen et al [13] have studied the 2060-T8/2099-T83 dissimilar joint of 2 mm thick plates, obtained by double-side synchronous laser welding with the ER4047 filler. It has been found that porosity in the WM has increased greatly with rising the laser power. Most pores have been found in the heat affected zone (HAZ) and dendritic branches in the WM, lowering the mechanical properties of the joint.

It has been reported in a series of papers by the authors [14–18] that laser welding of similar joints of plates from the Al-Mg-Li and Al-Cu-Li heat treatable alloys causes a fundamental change in their microstructures, as well as both chemical and phase compositions of the WMs. As a result, the mechanical properties of the joints have been lowered, but improved then after post-weld heat treatment (PWHT), which has included quenching and artificial aging.

Nevertheless, PWHT procedures vary for different alloys depending on their chemical composition, thicknesses of the joined plates, applied welding methods and parameters, initial tempering conditions, and (especially) the peak aging processes. For dissimilar welded joints of aluminum alloys, optimization of PWHT is challenging and some research in this direction is ongoing currently [19].

The microstructure and phase composition of the WM have to be known for developing PWHT procedures for dissimilar laser welded joints in order to improve their mechanical properties. In turn, they depend on both alloying system and properties of joined alloys, as well as non-equilibrium welding processes.

For dissimilar laser welded joints of the 1424 (Al-4.9Mg-1.65Li) and V-1461 (Al-2.7Cu-1.8Li-0.3 Mg) heat treatable alloys of the third generation, PWHT has not been optimized so far. This knowledge gap has been filled with the results of the present study of the microstructure and the mechanical properties (strength, microhardness, etc.) of such joints, both as-welded and after PWHT. Also, an approach for real-time optical diagnostics of a process of the formation of a heterogeneous material, based on laser emission spectroscopy, has been developed. Particular attention has been paid to research on spatial distributions of new phases formed via mutual diffusion of the alloying elements. For the first time, such investigations have been performed using synchrotron radiation. Diffraction studies have been carried out at the station of the fourth channel from the VEPP-3 storage ring.

Table 1
The chemical compositions of the investigated alloys (wt.%).

Grade and alloying system	Element						
	Al	Cu	Li	Zr	Sc	Mg	Zn
1424 Al-4.9Mg-1.65Li	Bal.	–	1.65	0.01	0.06	4.9	0.6
V-1461 Al-2.7Cu-1.8Li-0.3 Mg	Bal.	2.7	1.80	0.09	0.70	0.3	0.6

Table 2
The phase compositions of the investigated alloys.

Grade and alloying system	Phase composition	Main strengthening phases
1424 Al-4.9Mg-1.65Li	$\delta'(Al_3Li)$, $S_1(Al_2MgLi)$, $\beta'(Al_3Zr)$, Al_3Sc	$\delta'(Al_3Li)$
V-1461 Al-2.7Cu-1.8Li-0.3 Mg	$\delta'(Al_3Li)$, $\theta(Al_2Cu)$, T_1 (Al_2CuLi), $T_3(Al_5CuLi_3)$, β' (Al_3Zr), Al_3Sc, S'(Al_2CuMg)	$\delta'(Al_3Li)$, $T_1(Al_2CuLi)$

Table 3
The physical and mechanical properties of the investigated alloys.

Grade and alloying system	ρ, g/cm^3	λ, W/(m·K)	Cp, J/(kg·K)	σ_{UTS}, MPa	σ_Y, MPa	δ, %
1424, Al-4.9Mg-1.65Li	2.54	74	840	512	366	7.2
V-1461, Al-2.7Cu-1.8Li-0.3 Mg	2.64	92	910	550	470	10.1

2. Materials and methods

The 1424 (Al-4.9Mg-1.65Li; C_{Mg}/C_{Li} ~2.9) and V-1461 (Al-2.7Cu-1.8Li-0.3 Mg; C_{Cu}/C_{Mg} ~9 and C_{Cu}/C_{Li} ~1.5) heat treatable alloys [20–22] were chosen for the welding procedure. Their chemical and phase compositions are presented in Tables 1 and 2, respectively, based on the data reported in [6,15,23]. Table 3 includes their physical and mechanical properties, where ρ is density, λ is thermal conductivity, Cp is heat capacity, σ_{UTS} is the ultimate tensile strength, σ_Y is the yield point, and δ is elongation.

Plates with dimensions of 100 × 50 × 2 mm from both alloys were butt welded with the "Sibir-1" automated laser technological facility (Fig. 1), which included a continuous CO_2 laser with a power of up to 8 kW [24]. It had been developed at the Khristianovich Institute of Theoretical and Applied Mechanics SB RAS.

A welding head included a focusing ZnSe lens with a focal length of 254 mm, gas nozzles for shielding a weld pool from oxidation, and a mechanism for moving the lens along the beam axis. Both weld pool and root were shielded with helium supplied through the nozzles. The aluminum alloys possessed a high reflectivity, but their melting began at a certain threshold power density of 10^6 W/cm^2. After that, the reflection coefficient decreased and intensive melting started with the formation of a gas–vapor channel. This threshold power density was achieved under a certain combination of welding conditions (the radiation focusing, the laser power and the welding speed). When using the lens with the focal length of 254 mm and an output beam diameter of 30 mm, the minimum size of the focused spot was 180–200 μm for the applied laser BPP of 4.7 mm·mrad. With the used focusing system, the threshold power density was achieved at a laser power of ~1 kW.

For tensile tests, samples with dimensions of 100 × 10 × 2 mm were milled from the initial plates and the dissimilar welded joints according

Fig. 1. The "Sibir-1" automated laser technological facility.

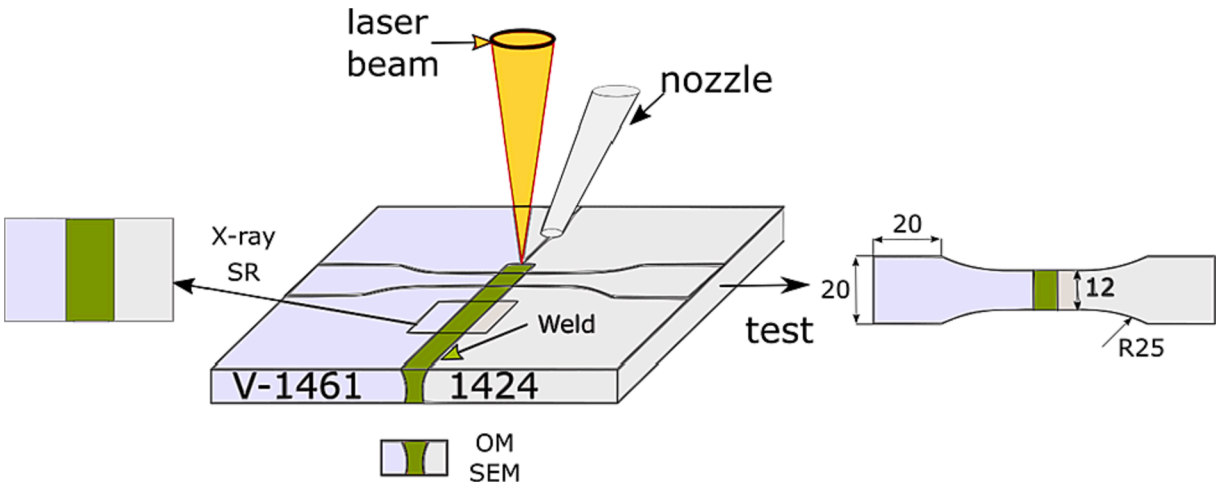

Fig. 2. The sample preparation scheme.

to the Russian state standard GOST 1497–84. In the welded samples, the weld axis was in their center perpendicular to the applied load direction. Fig. 2 shows a scheme of the sample preparation for the tensile tests, metallographic examinations by optical microscopy (OM) and scanning electron microscopy (SEM), as well as the phase analysis with synchrotron X-ray diffraction.

The tensile tests were performed with a 'Zwick/Roell' electromechanical universal testing machine. Elongation was measured with an extensometer at the 20 mm base, inside which was a weld about 1 mm wide.

For the metallographic examinations, the samples had been prepared with a grinding machine. At the finish stage, the 50 nm SiO_2 suspension was used. Since the alloys had significant difference in corrosion resistance the etching procedure included 2 stages. Initially, the samples were etched with Keller's reagent at room temperature for ~20 s. After that, the 1461 alloy was protected with an acid-resistant film and etching was continued at a temperature of ~40 °C for ~40 s.

Scanning electron microscopy (SEM) was performed with the Carl Zeiss EVO30 XVP microscope equipped with backscattered and secondary electron detectors and also with the Oxford Instruments X-Max 80 energy-dispersive X-ray (EDX) spectroscopic detector. The SEM procedure included 2 stages. At the first stage the samples were studied in a backscattered diffraction (BSD) image to reveal the chemical heterogeneity in the microstructure that helps to track the precipitations evolution. Since the etching procedure leads to the precipitations dissolving it was not applied at this stage. The second stage is aimed to reveal the grains shape evolution. To do that etching procedure was applied after that the samples were studied in a secondary electrons (SE) mode. Before study the samples were cleaned in distilled water with an ultrasonic probe after which the water was removed from the surface with a rubber blower.

The macrostructure of the welded joints was examined with an 'OLYMPUS LEXT 3000' optical microscope.

Phase analysis was carried out with the synchrotron X-ray diffraction

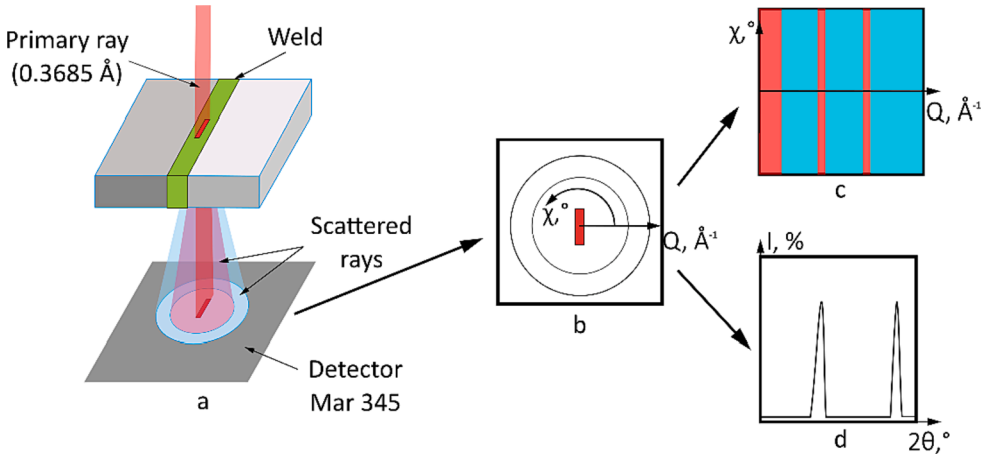

Fig. 3. The scheme of the diffraction data analysis: a – the signal accumulation process, b – the 2D diffraction ring patterns, c – the 2D diffraction patterns in the Cartesian coordinate system, d – the 1D diffraction pattern.

analysis at the Institute of Nuclear Physics at the station of the fourth channel of synchrotron radiation from the VEPP-3 storage ring [25]. A scheme of the experiment is shown in Fig. 3a. Monochromatic radiation with a wavelength of 0.3685 Å was used for research. When it had been accumulated, the beam possessed a rectangular cross section with dimensions of 100 × 400 μm. The detector had sizes of 345 × 345 mm and pixel dimensions of 100 × 100 μm. A sample-to-detector distance was 425 mm. At the applied low X-ray wavelength, the diffraction angles decreased, and all diffraction maxima were shifted to the region of small angles. The combination of "hard" synchrotron radiation and a flat two-coordinate detector (mar345) enabled to register the main set of diffraction maxima. The obtained patterns reflected the position and intensity of the diffraction rings, as well as the intensity distribution over the ring. The small range of angles and the high penetrating power of "hard" synchrotron radiation contributed the possibility of the transmission investigations in the Debye-Scherrer geometry. In this case, the entire volume of the sample through which the radiation passed, but not just the surface layers, contributed to the diffraction patterns.

The resulting 2D diffraction ring patterns (Fig. 3, b) were transformed into the Cartesian coordinate system for a more convenient analysis of the crystal orientations (Fig. 3, c). To analyze the peak locations, the 2D ring patterns were integrated into the 1D ones (Fig. 3, d). All data transformation was performed using the 'Area Diffraction Machine' software package (github.com/joshualande/AreaDiffractionMachine). Despite the high intensity of synchrotron radiation and a quite large (2 × 0.4 × 0.1 mm) area of the analysis, it was impossible to perform full profile analysis of the obtained patterns because of the extremely low volume fractions of the secondary phase particles, as well as due to a large number of different phases in the samples (up to five). Instead, the only positions and orientations of the peaks in the 2D patterns were taken into account (in cases when it was possible).

Angular positions of the observed phases were calculated using the crystallographic data at the Springer Materials website [26,27]. The space group of the S′($LiMgAl_2$) phase has not been reported yet, so the PDF-4 (ICDD 00-008-0283) card of Blank quality was used in this case.

The PWHT procedure included quenching and subsequent artificial aging, which was performed in a 'Carbolite' chamber furnace equipped with a temperature controller. Upon its optimization, the effect of quenching was studied, i.e. exposure of the samples at temperatures of 500–560 °C for 30 min followed by cooling in water, and artificial aging at temperatures of 120–200 °C for 8–40 h.

3. Results

3.1. Optimization of the laser welding parameters and the mechanical tests

Initially, the welding parameters were optimized, in particular the welding speed; the laser power; the focal spot diameter, depth and location, as well as the flow rate of the shielding gas in order to obtain sound joints without any external discontinuities, such as cracks, lack-of-fusion zones, undercuts, cavities, and porosity in the surface layer. The quality criterion for the WMs was the minimum porosity, as well as the width equality at the top and root surfaces of the X-shaped cross section with curved bevels of both joined plates [28]. Such cross sections contributed to the improvement of the mechanical properties of the dissimilar joints due to more symmetrical welds around their axis [29].

The range of the laser power levels was 1.6–3.5 kW, the laser focus depths were from –3 up to 0 mm, welding speed carried from 2 up to 4 m/min (33.3–66.7 mm/s), and the gas flow rates were within the range of 3–15 l/min.

At a welding speed of 8 m/min, a lack-of-fusion zone was observed. At its values lower than 2 m/min, weld pools were hydrodynamically unstable, overheating occurred and the molten metal moved to the root. At the optimum welding speed of 2 m/min, the dynamic stability of the molten metal flows in the weld pool was observed.

When the laser beam was focused on the weld pool surface, porosity was maximal but it decreased when the heat source displaced deeper. The optimal focus position was 3 mm, at which porosity was minimal.

The pore formation mechanisms were quite complex. The hydrodynamics of the molten metal flows on the wall of the gas–vapor channel had a dominant effect on the formed discontinuities [30]. At very low welding speeds, the gas–vapor channel was unstable because the laser beam affected its front wall that resulted in the displacement of the molten metal to the bottom of the weld pool. When moving the laser beam, the gas–vapor channel collapsed. At the same time, high welding speeds led to the molten metal flowing along the wall of the gas–vapor channel. However, penetration could not have occurred in this case. Respectively, it was necessary to maintain the heat input balance. The influence of the focus position in both keyhole and conductive modes of laser welding of aluminum alloys was theoretically considered in detail [31]. In the keyhole mode, the WM cross sections were calculated on the basis of the energy balance on the wall of the gas–vapor channel when temperature was taken equal to the boiling point of the alloys. A 3D temperature field of the weld pool was calculated considering the thermal conductivity. As a result, it was shown that rising the focus depth contributed to deeper penetration and, thereby, reduced porosity

Table 4
The energy parameters for the optimal welding modes.

Welded joint	t, mm	W, kW	V, m/min	Δf, mm	P, J/mm	P_{depth}, J/(s·mm)	E_{depth}, J/mm^2	E, J/mm^3
1424	1.5	2.9	4	–3	43.5	1933	29.0	40.28
V-1461	2	3.3	4	–3	49.5	1650	24.75	25.25
1424/V-1469	1.75*	3.2	4	–3	48.04	1828	27.45	26.4

Table 5
The mechanical characteristics of the welded joints.

Welded joint	σ_{UTS}, MPa	σ_Y, MPa	δ, %	k_1, %	k_2, %	k_3, %
1424	384	303	2.40	75	83	33
V-1461	341	333	0.70	62	71	7
1424/V-1461	262	234	0.83	45	49	12

in the WM. Its minimum values were in the keyhole mode. At a laser radiation power of 4 kW, overheating of the weld pool was observed, which caused cracking. On the contrary, the weld pool was underheated and the liquid flow was unstable, resulting in undercuts and lack-of-fusion zones at 2.5 kW. At the optimum laser power of 3.3 kW, molten metal flows were stable in the weld pool. Sound welds were formed with the optimal balance of the welding speed, the laser power and the focus position in the keyhole mode (Table 4). These data reflected the visual control results for both similar and dissimilar joints. In addition, Table 4 includes some important energy parameters, such as heat input $P = W/V$, energy per weld height $P_{depth} = W/t$, energy per linear area $E_{depth} = W/(t{\cdot}V)$, energy per unit volume of the molten material $E = W/(V{\cdot}t{\cdot}h)$, where W is the laser power, V is welding speed, t is the plate thickness, h is the mean weld width.

Table 5 presents the mechanical properties of the laser welded joints, where the k_i coefficients are ratios of their values to the initial levels of the BM (k_1 for the ultimate tensile strength, k_2 for the yield point, k_3 for elongation, respectively). For the dissimilar joint, the k_i coefficients were calculated relative to the 1424 alloy as the weakest one according to the data summarized in Table 3.

3.2. PWHT of the dissimilar welded joints

For the investigated alloys, the following heat treatment processes were developed: annealing, quenching and artificial aging. To achieve the maximum strength properties, it was necessary to obtain an intermediate microstructure via heating and cooling, which corresponded to the initial stages of decomposition of a supersaturated solid solution and the subsequent formation of strengthening phases in the WM. Since the dissimilar welded joints contained zones with very different chemical compositions, the development of PWHT procedures was a challenge. In this case, it was necessary to choose a mode suitable for both BMs and the dissimilar WM with an intermediate chemical composition. It was the circumstance that did not enable a priori to use the known PWHT procedures, which were applied in the industrial production of the aluminium–lithium alloys. Table 6 presents the reported PWHT conditions that enabled to improve the mechanical properties, previously deteriorated upon welding.

As a result of this study, a PWHT procedure, which included quenching and artificial aging, was optimized for the 1424/V-1461 dissimilar welded joints. Fig. 4 presents the σ_{UTS} ultimate tensile strength, σ_Y yield point and δ elongation values for the studied alloys and the dissimilar welded joint, as well as changes in their average levels depending on the quenching temperature.

According to Fig. 4, the optimal quenching temperature for the dissimilar welded joint was 530 °C, at which the maximum σ_{UTS}, σ_Y and δ values were observed. In this case, it was greater than those for both V-1461 and 1424 similar welded joints, which indicated variations of their microstructures and the phase compositions in comparison with the dissimilar one.

After quenching at the temperature of 530 °C for 30 min, subsequent artificial aging was carried out in two modes: at a temperature of 175 °C for 16 h and at 170 °C for 32 h, at which the maximum strength properties were achieved for the similar joints of the 1424 (Al-4.9Mg-1.65Li) and V-1461 (Al-2.7Cu-1.8Li-0.3 Mg) alloys, respectively.

Fig. 5 shows the σ_{UTS} ultimate tensile strength, σ_Y yield point and δ elongation values for the investigated alloys and the dissimilar joint, both as-welded and after the applied optimal quenching and artificial aging procedures.

According to Fig. 5, the optimal artificial aging mode included the temperature of 175 °C and the duration of 16 h for the dissimilar joint, at which the maximum σ_{UTS} ultimate tensile strength, σ_Y yield point and δ

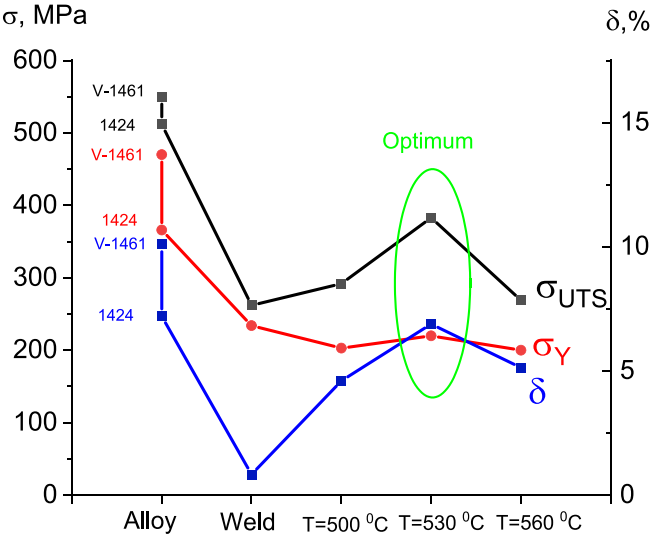

Fig. 4. The σ_{UTS} ultimate tensile strength, σ_Y yield point and δ elongation values for the BMs and the dissimilar joints, both as-welded and quenched at different temperatures.

Table 6
The mechanical properties of the similar welded joints [15,30].

Alloy	PWHT mode	As-welded	After PWHT	Ref.
1424	Quenching: 490 °C, 0.5 h Artificial aging: 175 °C, 16 h	σ_{UTS} = 384 MPa σ_Y = 303 MPa δ = 2.4 %	σ_{UTS} = 500 MPa σ_Y = 359 MPa δ = 6.6 %	[15]
V-1461	Quenching: 530 °C, 0.5 h Artificial aging: 170 °C, 32 h	σ_{UTS} = 341 MPa σ_Y = 333 MPa δ = 0.7 %	σ_{UTS} = 510 MPa σ_Y = 440 MPa δ = 8.7 %	[32]

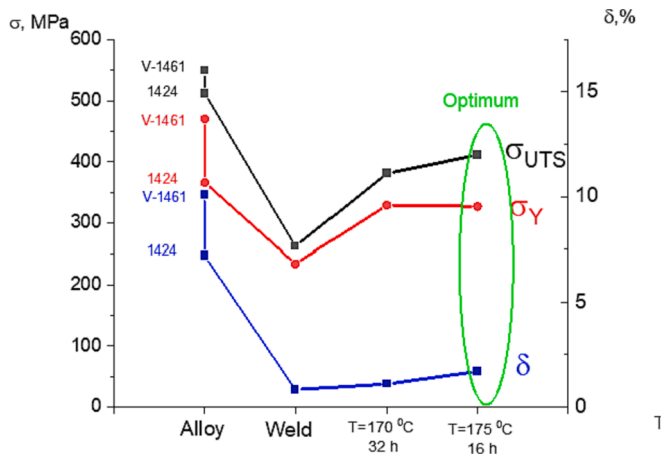

Fig. 5. The σ_{UTS} ultimate tensile strength, σ_Y yield point and δ elongation values for the investigated alloys and the dissimilar joint, both as-welded and after the applied optimal quenching and artificial aging procedures.

elongation values were achieved. It should be noted that it was the same as for the similar welded joint of the 1424 alloy.

Fig. 6 shows bar diagrams for the σ_{UTS} ultimate tensile strength, σ_Y yield point and δ elongation values, as well as the described above k_i coefficients for the studied alloys and their dissimilar joint, both as-welded and after PWHT.

Table 7 presents the mechanical properties of the dissimilar joint, both as-welded and after the optimal PWHT procedure, as well as the k_i coefficients. According to these data, the mechanical properties decreased upon welding, while quenching and subsequent artificial aging improved them. Moreover, quenching significantly enhanced both ultimate tensile strength and elongation, but artificial aging increased the yield point.

Fig. 7 shows microhardness distributions on the sample cross sections at both 1/3 of the height from the weld surfaces and its roots, measured with a microhardness tester at a load of 500 g. The tests were carried out on the as-welded sample, as well as after quenching at 530 °C for 30 min and after quenching at 530 °C for 30 min with subsequent artificial aging at 175 °C for 16 h.

As a result of welding, microhardness decreased in the WM. After quenching, it increased sharply compared to that in the HAZ, while microhardness decreased in both BMs. Artificial aging enhanced microhardness in the WM and the HAZ, especially near to the weld surface.

Based on the above-reported data, it could be stated that the maximum mechanical properties of the dissimilar joint were achieved after the following PWHT procedure: 1) quenching at 530 °C for 30 min, coinciding with that for the similar joint of the V-1461 alloy; 2) artificial aging at 175 °C for 16 h, at which the maximum strength characteristics were observed for the similar joint of the 1424 alloy. This fact testified to differences in the microstructures and phase compositions of the similar and dissimilar welded joints.

3.3. Microstructural studies

3.3.1. Macrostructure

Fig. 8, a shows the macrostructure of the dissimilar weld joint. The welded joint included the WM that transformed into the HAZs through a Fine eQuiaxed Zone (FQZ). In the WM (Fig. 8, d), the microstructure was of the dendritic type, while the HAZs consisted of columnar dendrites (Fig. 8, c and e). The formation of the FQZs along the WM boundaries was typical for the aluminum–lithium alloys. Such phenomenon was observed, for example, after welding some grades containing scandium, lithium and zirconium as alloying elements. [33,34]. In the keyhole mode, a molten boundary layer had been formed in the gas–vapor channel at its walls. Inside it, a flow rate of the molten metal had been negligible and some particles of intermetallic compounds containing refractory elements (for example, $Al_3(Li_x, Zr_{1-x})$ and Al_3Zr) had remained in the solid state. These particles could provide an interface for

Table 7
The mechanical properties of the dissimilar welded joint.

Parameter	σ_{UTS}, MPa	σ_Y, MPa	δ, %	k_1, %	k_2, %	k_3, %
As-welded	262	234	0.83	51.17	63.93	11.52
After quenching at 530 °C for 30 min	383	220	6.89	74.80	60.10	95.69
After quenching at 530 °C and subsequent artificial aging at 175 °C for 16 h	411	327	1.70	80.27	89.34	23.61

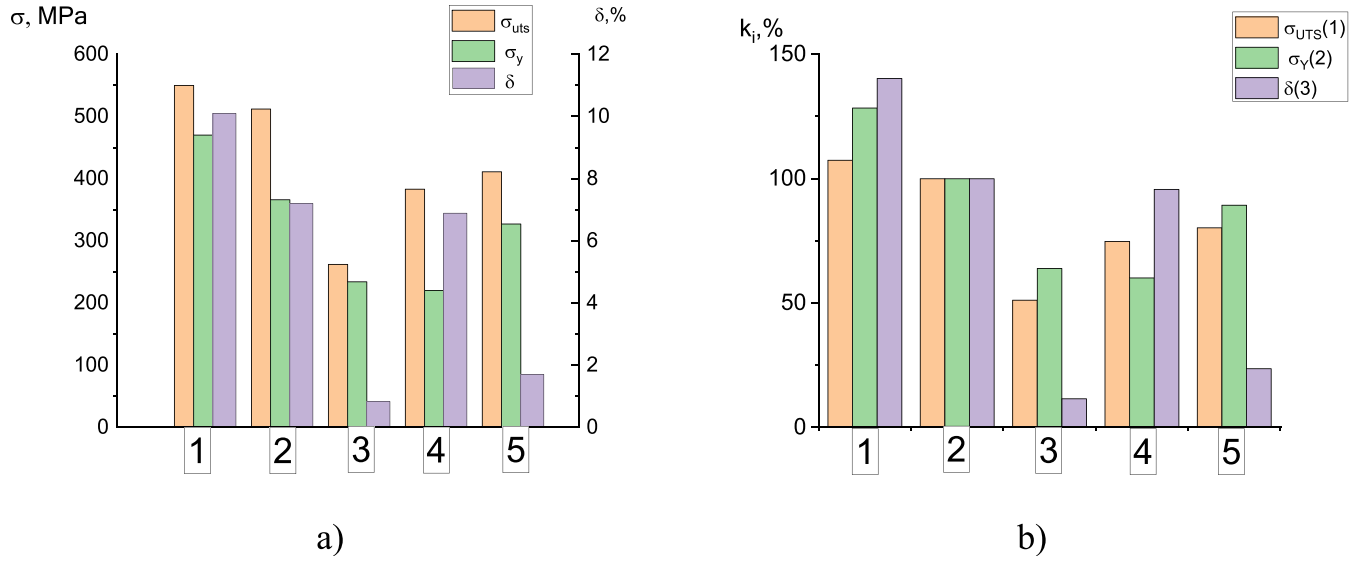

Fig. 6. The bar diagrams for the σ_{UTS} ultimate tensile strength, σ_Y yield point and δ elongation values, as well as the k_i coefficients for the studied alloys and their dissimilar joint, both as-welded and after PWHT: 1 – V-1461 alloy, 2 – 1424 alloy, 3 – as-welded joint, 4 – welded joint after quenching at 530 °C for 30 min, 5 – welded joint after quenching at 530 °C and subsequent artificial aging at 175 °C for 16 h.

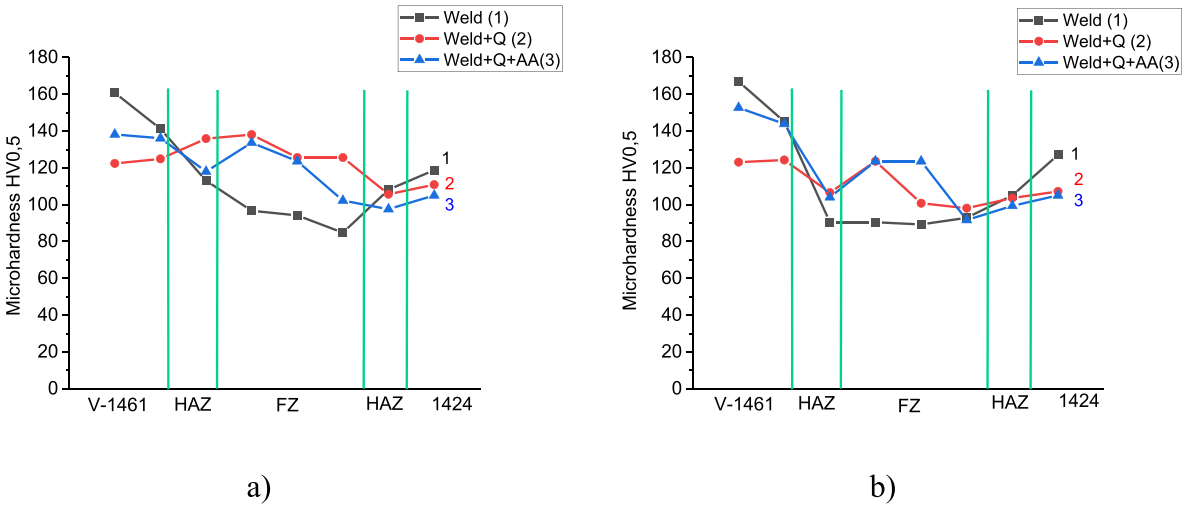

Fig. 7. The microhardness distributions on the sample cross sections before and after PWHT: a) 1/3 of the height from the weld surface, b) 1/3 of the height from the weld root(Q – quenching, AA – artificial aging).

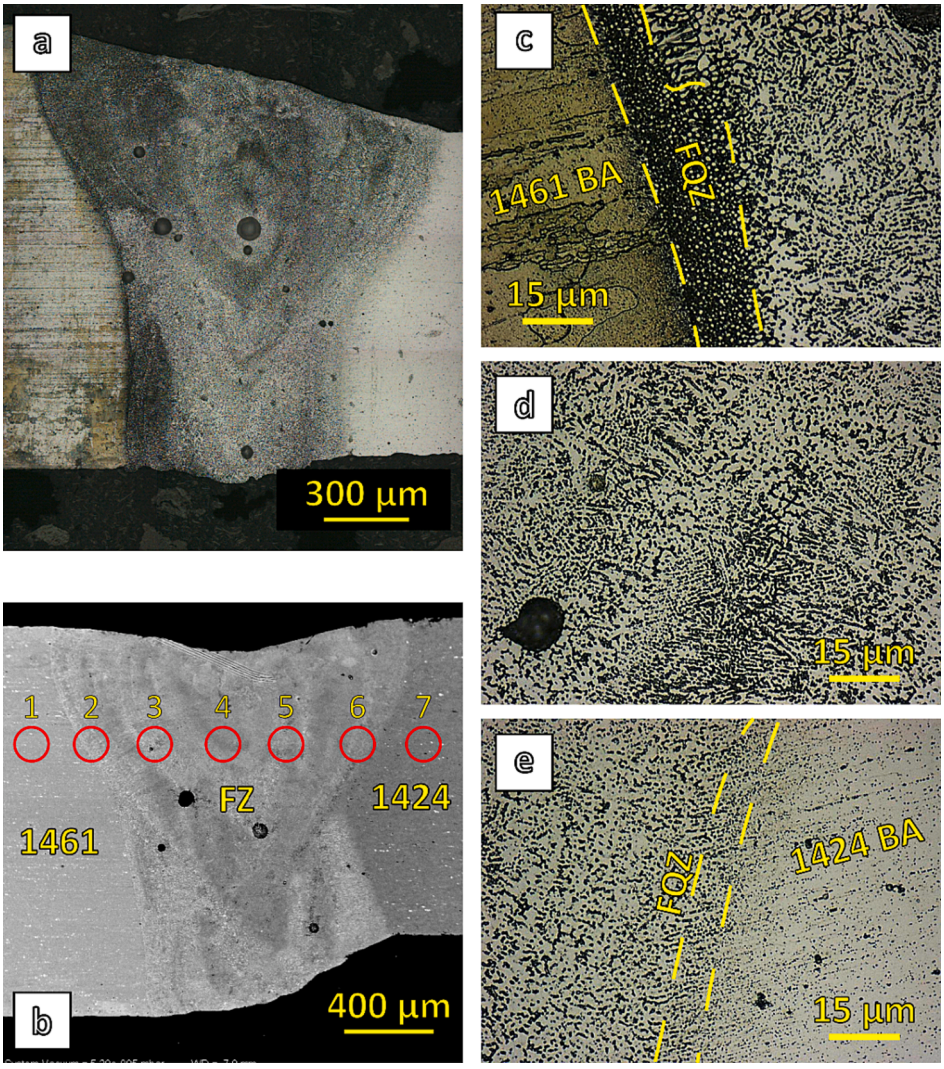

Fig. 8. The macrostructure of the dissimilar welded joint:

Table 8
The EDX analysis results at the areas highlighted in Fig. 8.

Spectrum	Al, at. %	Cu, at. %	Mg, at. %	Mn, at. %	Zn, at. %	Comments
1	97.87	1.27	0.57	0.08	0.21	*V-1461 BA*
2	97.42	1.17	1.08	0.08	0.25	*FQZ near V-1461*
3	97.25	1.02	1.41	0.08	0.24	*FZ*
4	96.80	0.83	2.06	0.07	0.24	*FZ*
5	96.41	0.73	2.56	0.08	0.22	*FZ*
6	94.86	0.34	4.42	0.07	0.31	*FQZ near 1424*
7	94.06	—	5.53	0.10	0.31	*1424 BA*

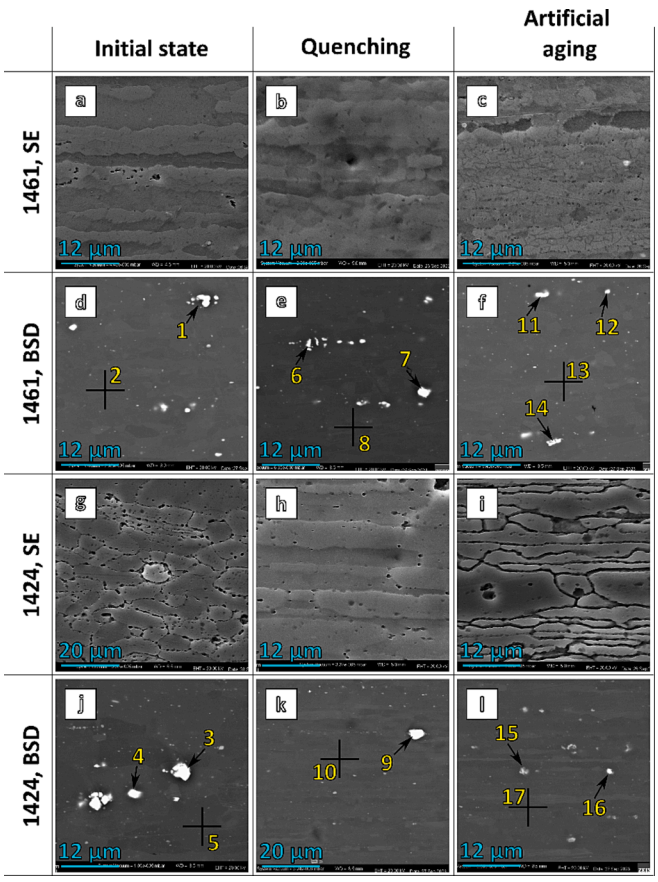

Fig. 9. SEM images (both SE and BSD modes) of the microstructure of the BMs with the highlighted areas of the performed EDX analysis.

the beginning of heterogeneous solidification.

On the V-1461 alloy side, the FQZ width was about 15 μm, while it was less than 10 μm on the 1424 one. According to Table 1, the V-1461 alloy contained zirconium and scandium in the amount of 0.09 and 0.70 wt%, respectively, but their concentrations were only 0.01 and 0.06 wt % in the 1424 one. This difference by an order of magnitude had been the reason for the formation of such a clear FQZ on the side of the V-1461 alloy, but rather blurry one on another side.

The WM possessed a distinct dendritic microstructure of various dimensions and shapes. On the 1424 alloy side, it consisted of disordered equiaxed dendrites 10–15 μm in size, but it included columnar ones with dimensions of 5–10 μm in the middle and on the V-1461 alloy side.

The EDX analysis results, presented in Fig. 8, b and Table 8, enabled to conclude that the chemical composition of the WM greatly depended on the location of the investigated area. Thus, the copper content decreased in the direction from the V-1461 alloy to the 1424 one. However, even near the 1424 alloy (spectrum 6), some amount of copper was found despite the fact that it was absent in the BM (spectrum 7). Magnesium demonstrated the same behavior but in opposite direction, i.e. the WM contained its lower amount it was present in the 1424 alloy, and reduced further towards the V-1461 alloy side Fig. 9.

a – a general view (optical image), b – a SEM image (BSD) with the highlighted areas of the performed EDX analysis, c – the FQZ at the 1461 alloy side (an OM image), d – the central part of the WM (an OM image), e – the FQF at the 1424 alloy side (an OM image).

3.3.2. *The microstructures of the BMs*

Both 1424 and V-1461 alloys consisted of elongated grains (Fig. 9, a–c and g–i) with precipitates of several types (Fig. 9, d–f and j–l). Large ones (1–4 μ min size) were characterized by the presence of numerous elements, such as iron, manganese, nickel, silicon and even calcium, which was an inevitable result of contamination during their industrial production. Copper was also found in particles. Few rather large particles (~3 μm) rich in titanium, zirconium and scandium were observed as well (Fig. 9, e, spectrum 9 in Table 9). The second type of precipitates were much smaller (<1 μm) and reflected as tiny bright spots in the SEM images obtained in the BSD mode (Fig. 9). Since the size of analysis area during EDX (~7 μm in this case) exceeded the distance between these particles, it was not possible to determine their chemical composition. The chemical composition of grains in both materials did not change significantly during PWHT (Table 9, spectra 2, 8, 14 and 5, 10, 17). Accordingly, these large particles did not affect the transformations upon hardening and aging, i.e. they did not dissolve in the matrix and, therefore, were not segregate during subsequent artificial aging.

3.3.3. *The microstructure of the WM*

Fig. 10 shows SEM images in which it was possible to trace the dynamics of changes in the morphology and sizes of grains caused by quenching. The as-welded WM consisted of columnar dendrites (Fig. 10, d and j), while its central part included equiaxed dendrites (Fig. 10, g). After quenching, no dendrites were observed, but grains were columnar or equiaxed (depending on their location) with convex boundaries in most cases (Fig. 10, e, h and j).

Near to the 1424 alloy, the FQZ was characterized by a dendritic microstructure (Fig. 10, m), changed similarly to the WM after quenching (Fig. 10, n). At the 1461 alloy side, the FQZ did not change upon quenching, since it initially had not included any dendrites (Fig. 10, a and b).

In all examined areas, no significant changes were observed after artificial aging. However, at magnesium-rich areas of the WM, some variations in their sensitivity to etching should be noted. After quenching and subsequent artificial aging, the microstructure was revealed more clearly (Fig. 10, l and o) than after quenching only (Fig. 10, j and n). This phenomenon could be explained by different contents of magnesium in the aluminum solid solution due to its release into the S' phase upon artificial aging. The solid solution with a lower magnesium content was characterized by decreased corrosion resistance, which was manifested in the more pronounced microstructure after etching.

SEM images of the WM obtained in the BSD mode showed significant amounts of the copper-rich eutectic between dendritic grains throughout its as-welded volume (Fig. 11, a, d, g, j and m). After quenching, it was not found, so the only chemical inhomogeneities were some particles similar to those observed in the BMs metals, but of different chemical compositions. They mainly included copper and magnesium (in addition to aluminum), while iron, manganese and nickel were almost absent. This phenomenon could be explained by their smaller size (~2 μm in the WM versus ~4 μm in the BMs), due to which the average composition of the analyzed region (width of ~7 μm) turns out to be poorer in iron, nickel and manganese (Table 7) in comparison with those in the BMs (Table 6). It should be noted that smaller particles were preferentially located along the grain boundaries in the WM (Fig. 11) in contrast to the BMs (Fig. 9).

Table 9
The EDX analysis results at the areas highlighted in Fig. 9.

Spectrum	Al, at.%	Cu, at.%	Mg, at.%	Fe, at.%	Mn, at.%	Ni, at.%	Zn, at.%	Sc, at.%	Other, at.%	Comments
1	89.97	6.51	—	2.55	—	0.38	0.14	—	—	
2	98.03	1.20	0.58	—	—	—	0.19	—	—	*Al grain*
3	80.45	—	1.30	13.45	3.93	0.64	—	—	*Si:* 0.23	
4	81.98	—	2.60	11.51	3.24	0.49	—	—	*Si:* 0.18	
5	93.97	—	5.63	—	0.07	—	0.33	—	—	*Al grain*
6	97.35	1.71	0.52	0.19	0.23	—	—	—	—	
7	81.37	11.79	—	5.40	0.85	0.59	—	—	—	
8	98.10	1.15	0.52	—	—	—	0.24	—	—	*Al grain*
9	82.26	—	2.21	—	—	—	0.23	4.01	*Zr:* 9.89 *Ti:* 1.38	
10	94.48	—	5.52	—	—	—	—	—	—	*Al grain*
11	87.18	8.72		1.38	0.52	0.22	0.19	0.19	*Ca:* 1.60	
12	97.51	1.52	0.49	0.18	0.07	—	0.22	—	—	
13	98.28	1.16	0.49	—	0.07	—	—	—	—	*Al grain*
14	91.11	6.55	—	0.33	0.44	0.09	0.20	—	*Ca:* 1.28	
15	90.74	—	5.34	1.88	1.57	0.16	0.16	—	*Si:* 0.15	
16	89.04	—	5.09	3.37	1.90	0.19	0.12	0.08	*Si:* 0.21	
17	94.04	—	5.76	—	—	—	0.20	—	—	*Al grain*

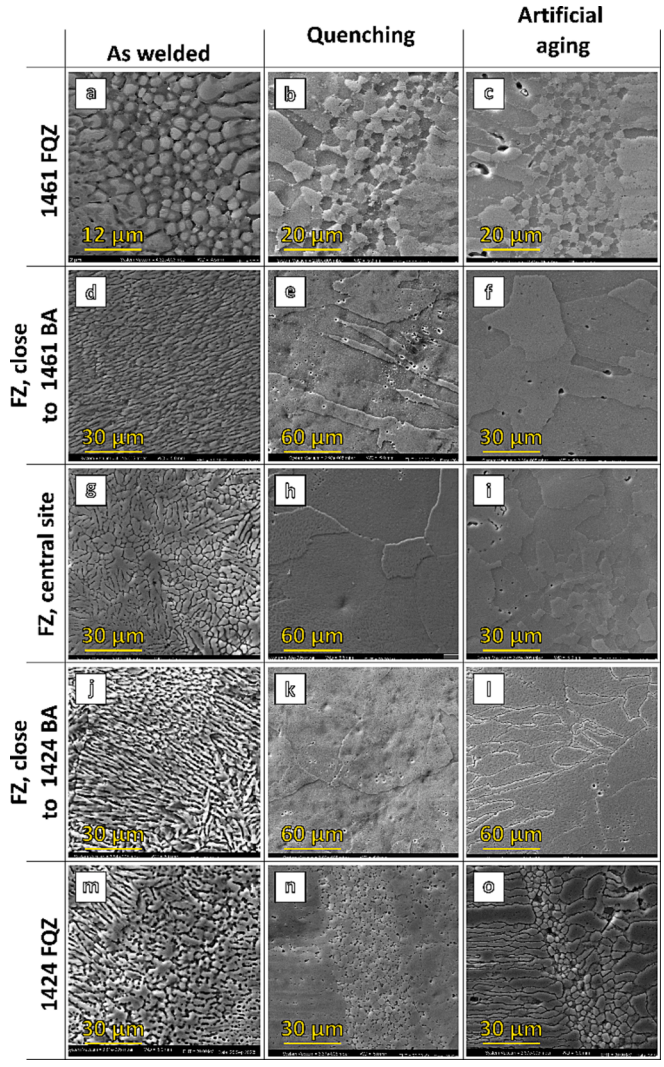

Fig. 10. The SEM images of the WM obtained in the SE mode (as-welded, after quenching and after quenching and subsequent artificial aging): a–c – the FQZ at the V-1461 alloy side, d–l – different parts of the WM, m–o – the FQZ at the 1424 alloy side.

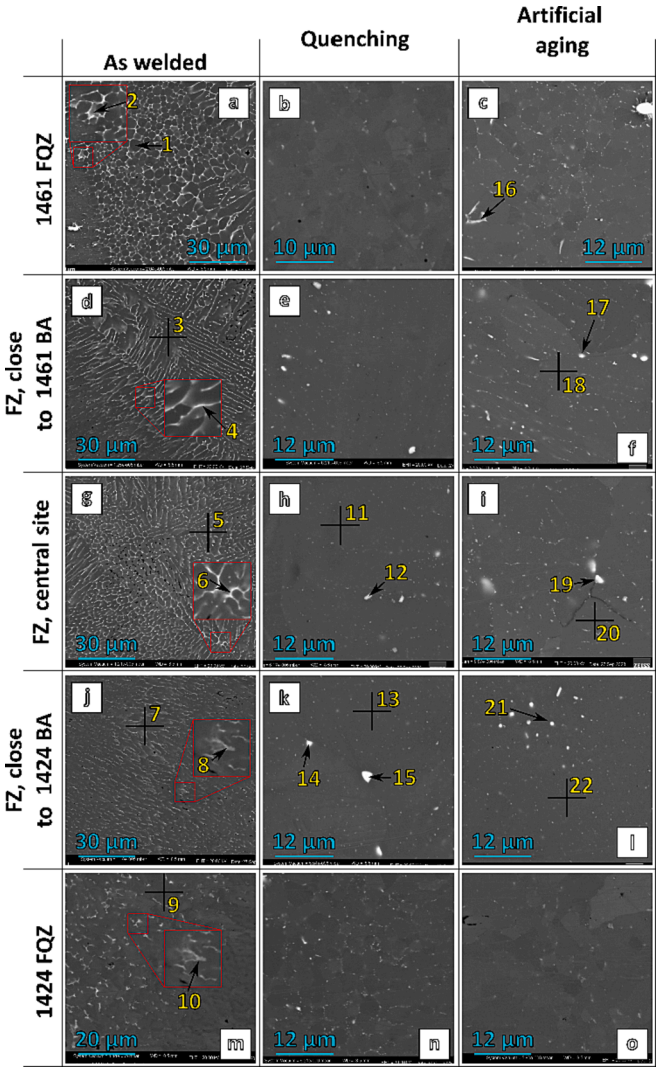

Fig. 11. The SEM images of the WM obtained in the BSD mode (as-welded, after quenching and after quenching and subsequent artificial aging): a–c – the FQZ at the V-1461 alloy side, d–l – different parts of the WM, m–o – the FQZ at the 1424 alloy side.

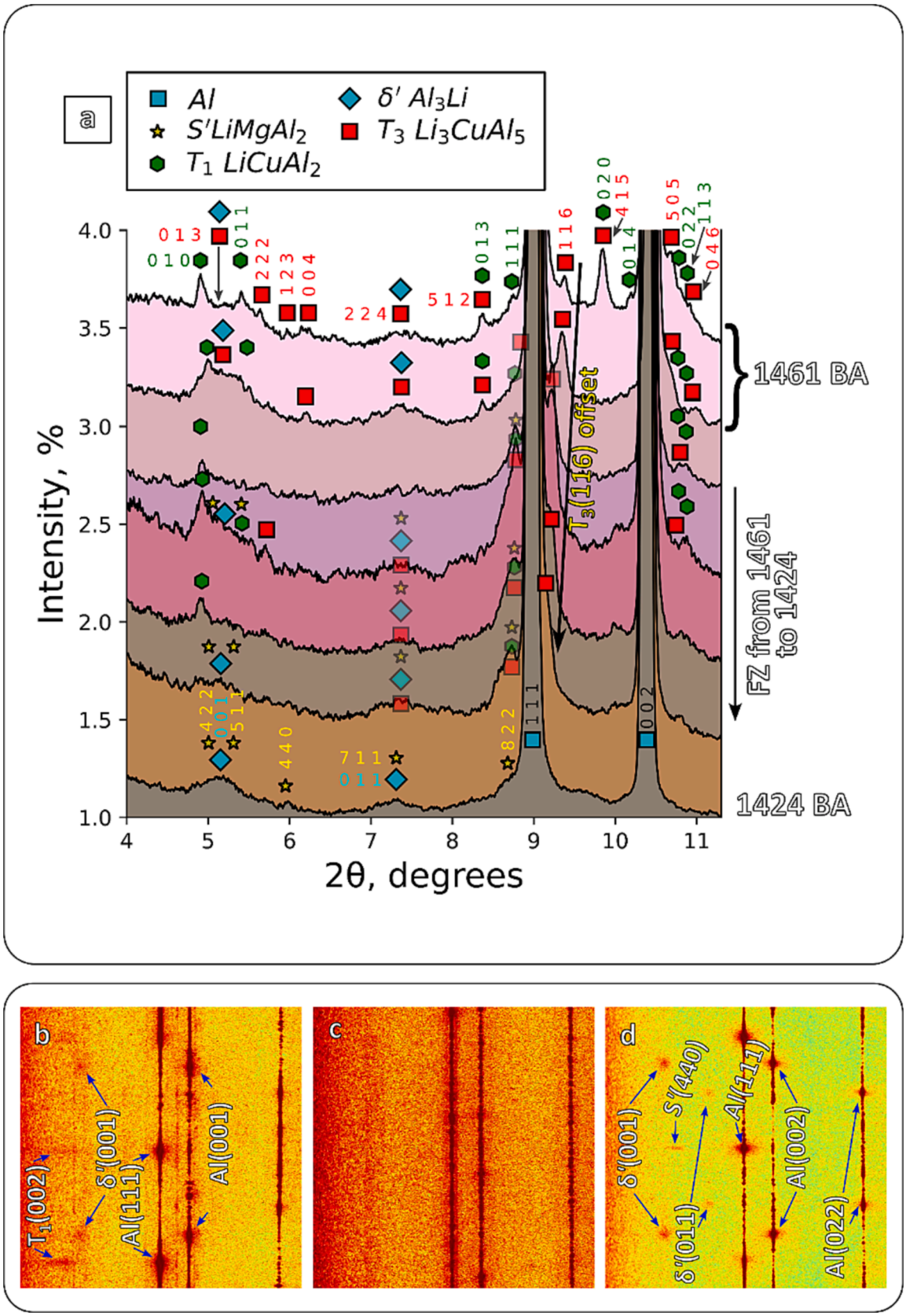

Fig. 12. The X-ray diffraction data for the as-welded sample: a – the 1D diffraction patterns, b–d – the 2D diffraction patterns in the Cartesian coordinate system at the V-1461 BM, the center of the WM, and the 1424 BM, respectively.

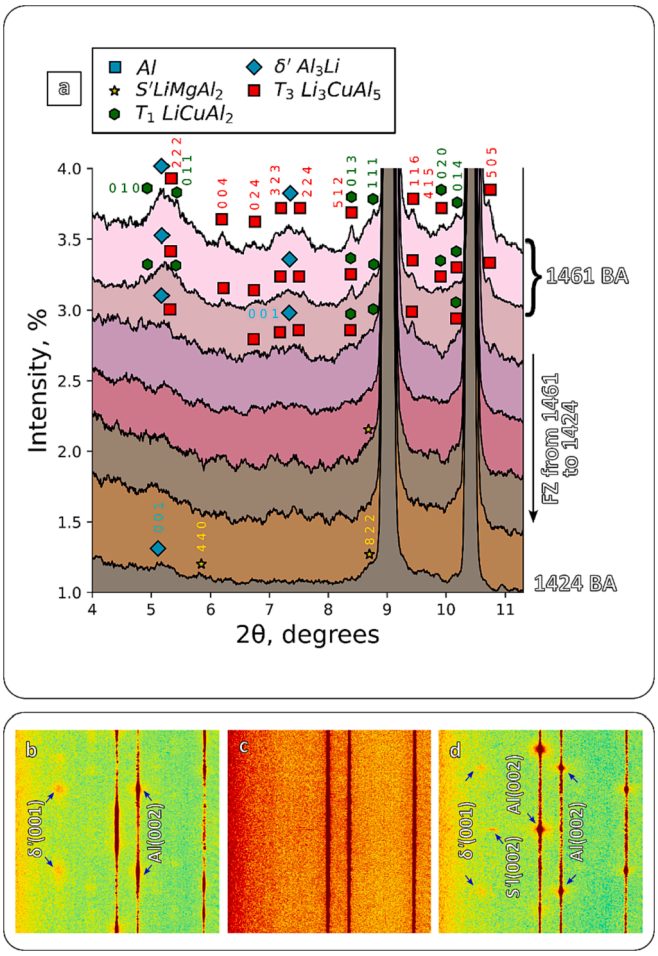

Fig. 13. The X-ray diffraction data for the sample after quenching: a – the 1D diffraction patterns, b–d – the 2D diffraction patterns in the Cartesian coordinate system at the V-1461 BM, the center of the WM, and the 1424 BM, respectively.

3.3.4. *Synchrotron X-ray diffraction*

According to the 1D diffraction patterns shown in Fig. 12, a, the 1424 alloy contained the S′(Al_2LiMg) precipitations, while the V-1461 grade included the T_1(Al_2CuLi) and T_3(Al_5CuLi_3) ones. Also, both alloys contained the δ′Al_3Li phase. Since both welded plates had been produced by cold rolling, grains of aluminum and secondary phases were preferentially oriented. This fact was indicated by the presence of maxima in the Al(1 1 1) and Al(1 1 0) 2D patterns (Fig. 13, b and d).

In Fig. 12, b, the (0 0 2) peaks of the T_1 phase were very wide in the Q direction that meant that their particles were smaller in the ⊥(0 0 2) direction. Its width at half height is ~1.5° by which the particle size of the T_1 phase in the ⊥(0 0 2) direction can be roughly estimated as ~2 nm (according to the Scherrer equation). Also, it's clearly seen that the T_1 (0 0 2) peaks repeat the Al (1 1 1) maxima direction along the *chi* axis which means the T_1 (0 0 2) || Al (1 1 1) orientation relationship in this case. It should be noted that similar both size and mutual orientation were reported in [35]. The secondary phase S′ in 1424 alloy has a specific orientation relationship S′(4 4 0) || Al (1 1 1) which is demonstrated in Fig. 13d. Additionally, in the cases of both BA there are δ′Al_3Li (0 0 1) || Al (0 0 2), δ′Al_3Li (0 1 1) || Al (0 2 2) etc. orientation relationships (Fig. 13 b and d) which appears due to the fact that δ′ phase is a result of a local (Al) solid solution ordering which results in (Al) Fm-3m → δ′ Pm-3 m transformation with almost the same cell parameter [36].

The WM possessed no texture (Fig. 12, c), so nothing could be reported about its orientation relationships. However, the 1D diffraction pattern demonstrated the presence of all secondary phases found in both BMs (Fig. 13, a). The δ′(Al_3Li) phase was practically absent in the WM, but the peaks of the all other ones were sharper, reflecting larger sizes of their particles. In the WM, the peaks of the T_3 phase shifted, and this effect intensified closer to the 1424 alloy (as an example, the shifted T_3 (1 1 6) peak in Fig. 13, a). This behavior could be caused by a change in the chemical composition of this phase due to differences in the precursor liquid in the direction from the V-1461 BM to the 1424 one.

After quenching, both BMs retained their texture (Fig. 13, b and d). The δ′(Al_3Li) phase retained its orientation relationships (Fig. 13, b and d). The S' phase also possessed the S'(4 4 0) || Al (1 1 1) relationship (Fig. 13, d). The 1D diffraction shown in Fig. 14, a enabled to conclude that quenching led to the additional formation of the δ′ phase the V-1461 BM, while both T_1 and T_3 ones were unchanged. The 1424 BM showed a different behavior, i.e. the peaks of the δ′(Al_3Li) phase were not found but the S' ones remained the same. In the WM, all peaks were lower, so it was impossible to accurately identified them. This fact indicated that most of the secondary phases were dissolved in the aluminium matrix, which was the aim of the quenching procedure.

Aging process resulted in the formation of all the secondary phases in the weld pool (Fig. 14a). δ′Al_3Li peaks can be clearly seen in each 1D pattern. Additionally, it still keeps the δ′Al_3Li (0 0 1) || Al (0 0 2) orientation relationship in cases of the both base alloys (Fig. 15 b and d). The rest phases didn't obtain such a significant rise in their peaks' intensity. However, the presence of them in 1D diffraction patterns in welding pool site indicates their formation in the result of the aging process.

4. Discussion

EDX analysis (Table 7) showed that the eutectics between the dendritic grains in as welded material contain significant amount of Cu. Together with synchrotron X-ray diffraction results one can conclude that the eutectics consists of at least τ_1 and τ_3 phases (in addition to Al).

PWHT significantly changed the microstructure and the phase composition of the V-1461/1424 dissimilar welded joint, which improved the mechanical properties. First of all, the quenching procedure changed the grains shape from dendritic to round one (Fig. 10). The eutectics between the dendritic grains was dissolved (Fig. 11). However, the eutectics wasn't fully dissolved that can be seen by the presence of some peaks in diffraction patterns in addition to the Al ones (Fig. 14) although they are not so obvious as in the as welded material (Fig. 13). Diffraction patterns of the aged material (Fig. 15) showed the precipitation of δ′, τ_1, τ_2 and S′ phases which was the aim of this procedure. Despite this, no additional particles were observed by SEM investigation. It means that the secondary phases were smaller then ones that can be observed by the applied equipment.

Before quenching the dendritic grains were surrounded by Cu-rich eutectics. Its formation led to the purification of the Al dendrites which was demonstrated by EDX analysis (Table 7). Such a microstructure makes the welded material some kind of inverse composite with softened "reinforcements" surrounded by hard and brittle matrix. Obviously, such a microstructure cannot provide the best mechanical performance (Fig. 17) that manifests itself in ultimate and yield tensile strength and elongation drop down to 262 MPa, 234 MPa and 0.83 % respectively (51, 63 and 12 % of the properties of 1424 alloy).

Significant increase of the elongation (up to 6.89 % or 96 % of 1424 alloy's value) can be explained by the disappearance of the brittle eutectics at the grain boundaries in welded material. Since this procedure aims (and the aim was achieved) to dissolve the precipitations in supersaturated solid solution there is no surprise that we didn't achieve high ultimate and yield tensile strength (383 and 220 MPa or 75 and 60 % of 1424 alloy's values respectively). However, the disappearance of the eutectics between grains boundaries significantly increased ultimate tensile strength.

Aging procedure led to the formation of all the secondary phases of the both initial alloys in the weld material. It led to an additional increase of ultimate tensile strength up to 411 MPa (80 % of 1424 alloy's

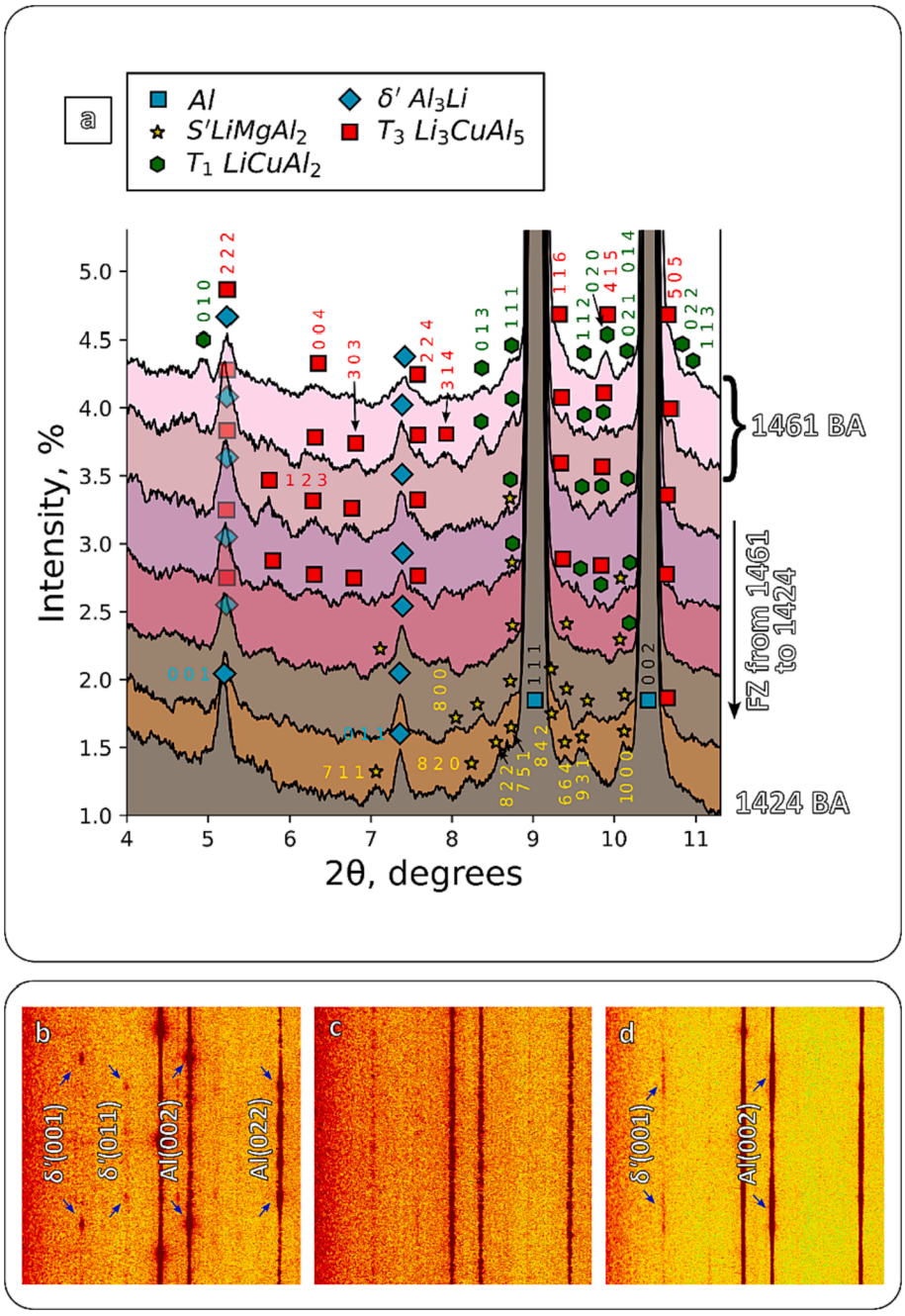

Fig. 14. The X-ray diffraction data for the sample after quenching and subsequent artificial aging: a – the 1D diffraction patterns, b–d – the 2D diffraction patterns in the Cartesian coordinate system at the V-1461 BM, the center of the WM, and the 1424 BM, respectively.

value). However, the most important impact of aging procedure was a significant growth of yield tensile strength which increased up to 327 MPa (89 % of the 1424 alloy's value). In contrast, the elongation value dropped down to 1.70 % (24 % of the 1424 alloy's value). Such a behavior can be explained by excessive hardening by the precipitations which can be observed by the diffraction patterns (Fig. 15).

Due to the fact that the majority of the alloying elements of the alloys are concentrated in the eutectics, the dendrites in the weld material were poorly alloyed (Fig. 11, Table 10). Lack of these elements was the reason of the Al grains softening that is why the microhardness decrease. Quenching procedure led to the eutectics disappearance together with the formation of the supersaturated solid solution in the Al grains. The increase of the alloying elements concentration in the solid solution led to the microhardness growth. Aging procedure aimed to create new precipitation from solid solution. Together with the synchrotron X-ray diffraction analysis (Fig. 15) microhardness tests also show the precipitation presence by the additional microhardness increase. Similar behavior was demonstrated in [37].

In addition, some important features of the formation of the WM due to the difference in the thermal conductivity values for the joined alloys should be noted, which contributed to the above-mentioned phenomenon.

The solidification of the WM was significantly affected by the time-dependent thermal mode of laser welding. At the liquid–solid interface, the formation of the microstructure was determined by two key parameters: the G temperature gradient and the R solidification rate. The formed dendritic structure depended on the G/R ratio. Therefore, the WM consisted mainly of dendritic grains, since the welding process

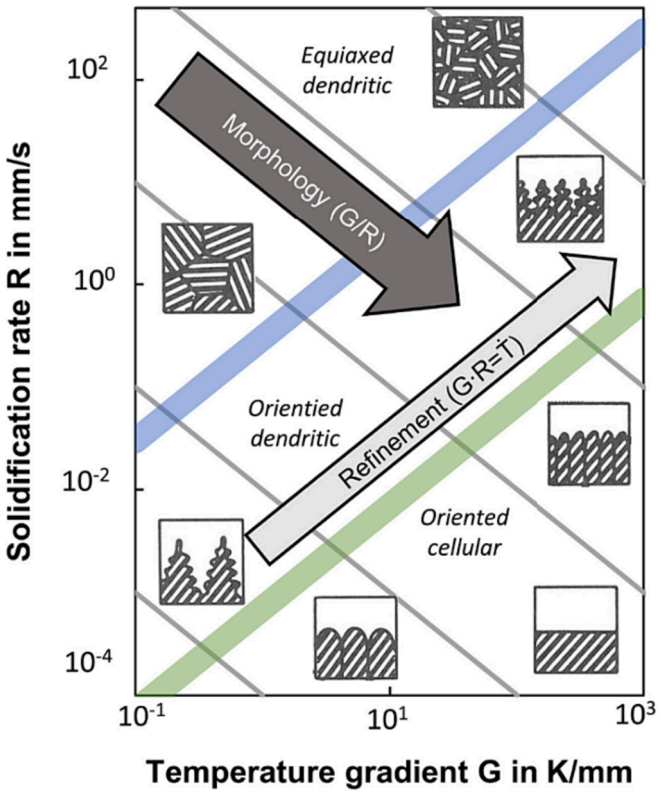

Fig. 15. The map of changes in the morphology of the microstructure formed in the WM, depending on the G and R parameters. The insets schematically show the resulting grain structure in the WM [38].

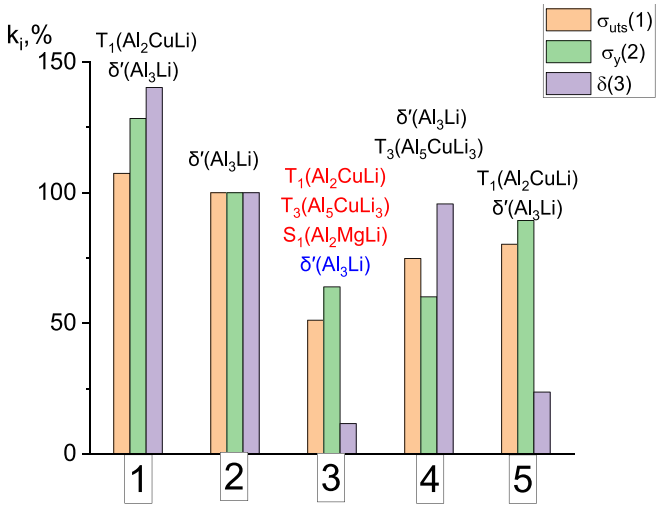

Fig. 16. A scheme of the phase transformations and the changes in the mechanical properties, as well as the k_i coefficients for the dissimilar joint, both as-welded and after PWHT: 1 – the V-1461 alloy, 2 – the 1424 alloy, 3 – the as-welded joint, 4 – the welded joint after quenching at 530 °C for 30 min, 5 – the welded joint after quenching at 530 °C and subsequent artificial aging at 175 °C for 16 h.

was characterized by a very high R solidification rate.

The relationship of the dT/dt cooling rate with the above parameters was $dT/dt = G{\cdot}R$. Thus, the G/R ratio determined the morphology of the resulting grain structure. An increase in the cooling rate accelerated the grain nucleation process, decreasing their sizes. Therefore, the $G{\bullet}R$ multiplication determined the grain sizes. The G and R values could be expressed as follows:

$$G = \sim NT{\cdot}n \tag{1}$$

$$R = V{\cdot}i{\cdot}n \tag{2}$$

where n was a unit normal vector to the liquid–solid interface, i was a unit velocity direction vector.

According to [38], the following expression was obtained for the temperature gradient on the liquidus isotherm:

$$G(P,v) = \frac{dT}{dt} = 2\pi\frac{(T_{liq}-T_0)^3}{\eta_{abs}^2 * P_{Depth}^2}\lambda V\rho C_p \tag{3}$$

and it was for a cooling rate

$$\frac{dT}{dt} = GR = 2\pi\frac{(T_{liq}-T_0)^3}{\eta_{abs}^2 * E_{Depth}^2}\lambda\rho C_p \tag{4}$$

where T_{liq} was the liquidus temperature, η_{abs} was the radiation absorption coefficient, λ was thermal conductivity, C_p was heat capacity, ρ was density, P_{Depth} was the laser beam specific power equal to the ratio of the P laser power to the S welding depth, $E_{Depth} = P/SV$ was the linear laser energy per welding depth.

The temperature changes depended on the λ thermal conductivity and the E_{Depth} linear laser energy per welding depth. Fig. 15 shows a map of changes in the morphology of the microstructure formed in the WM, depending on the G and R parameters according to [38–41].

Table 11 presents the estimated parameters, determining the morphology of the final grain structure, the G/R solidification mode and the $G{\cdot}R$ cooling rate for the similar welded joints, calculated using Formulas (3) and (4). The parameters of both BMs and the optimal welding conditions were taken from Tables 3 and 4, while the absorption coefficient of laser radiation was considered as 0.8 according to [38].

For the dissimilar welded joint, it was difficult to evaluate these parameters, because it was necessary to take into account the thermophysical properties of the material according to Equations (3) and (4). In the studied case, a new material had been formed in the WM as a result of laser welding and, accordingly, an investigation of its thermophysical properties was a separate task.

Variations in the cooling rates and the solidification modes were due to the differences in the thermal conductivities and the heat capacities for the studied alloys. This apparently determined the distinctions of the dendritic microstructure in the HAZs on both sides and in the WM.

In the WM and the HAZ at the V-1461 alloy side, there was the increased copper concentration in bright areas, while they were lower in their solid solutions compared to the BM. From the 1424 alloy side, the elevated magnesium concentrations were observed, gradually decreasing towards the V-1461 alloy. These circumstances could be caused by the non-equilibrium solidification with the release of the alloying elements. Upon rapid cooling of the WM, diffusion in the solid state did not have time to occur, while it could be completed in the weld pool. Respectively, the compositions of the solidified dendrites changed slightly, since they were mainly determined by those in the liquid state. In this case, the solidification process began at the maximum temperature in the weld pool with the precipitation of α-Al crystals, which contained the alloying elements, rising the melting point. As a result, supersaturated solid solutions of the alloying elements were formed and impurities were unevenly distributed over the dendrite volumes in such eutectic and hypereutectic systems [37,38].

Thus, the above processes had occurred in the weld pool, including the dissolution of the strengthening phases in the solid solution, the localization of the alloying elements mainly at the boundaries of the dendritic subgrains as a result of the non-equilibrium solidification, as well as the formation of the $T_1(Al_2CuLi)$, $T_2(Al_5CuLi_3)$, $S_1(Al_2MgLi)$, phases, depending on the predominant alloying with copper or magnesium. This led to the decrease in the ultimate tensile strength of the

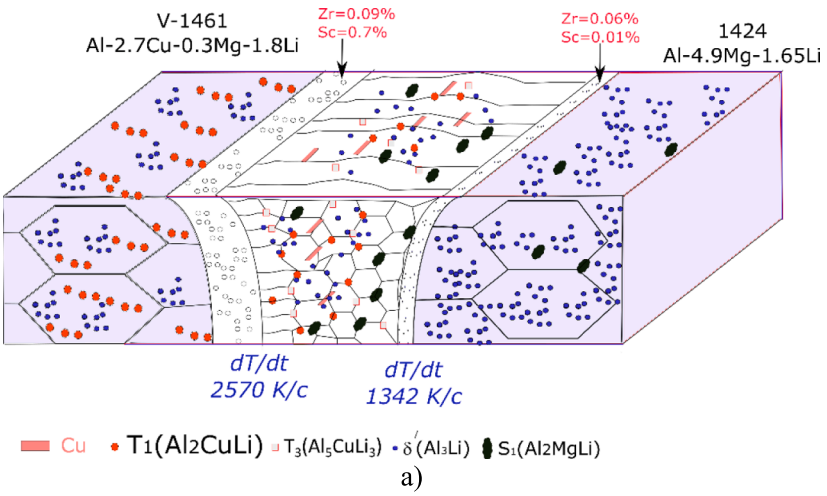

a)

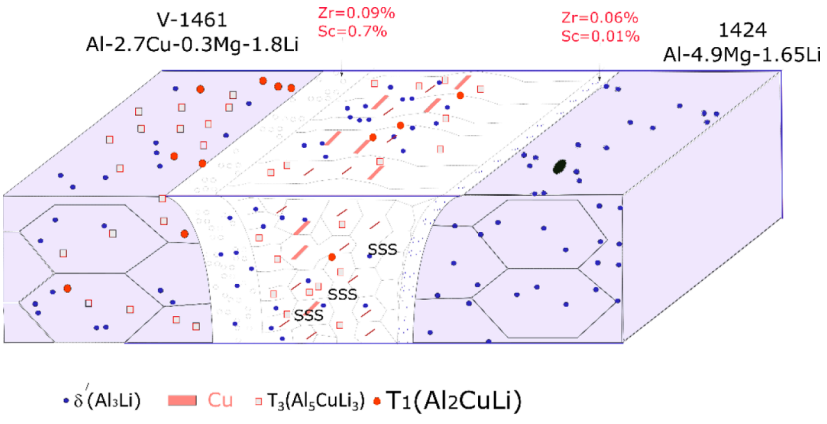

b)

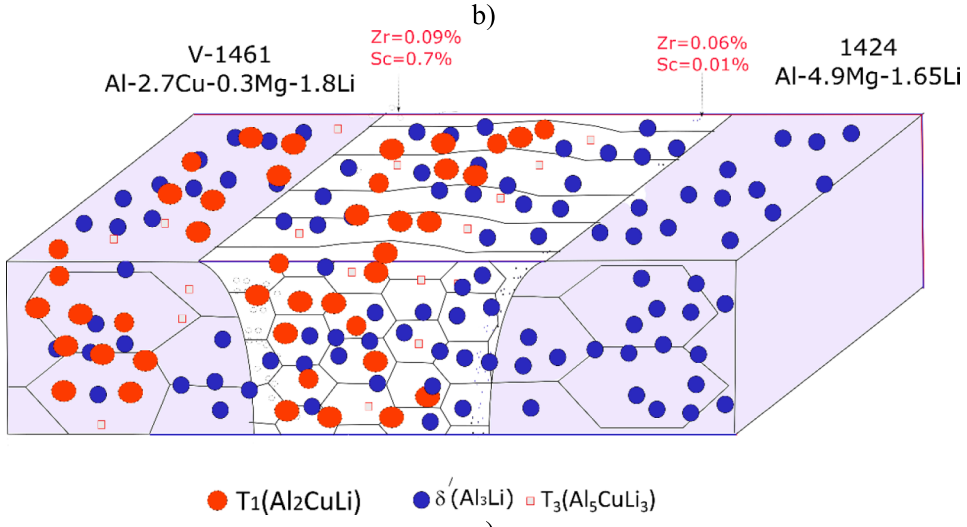

c)

Fig. 17. The evolution of the microstructures and the phase transformations upon laser welding (a), quenching at 530 °C for 30 min (b), as well as quenching at 530 °C and subsequent artificial aging at 175 °C for 16 h (c).

dissimilar welded joint down to the level of 50–60 % of that for the 1424 alloy as the weakest one.

Subsequent quenching at 530 °C caused the formation of the $\delta'(Al_3Li)$ phase with lowering the intensity of peaks of the $T_1(Al_2CuLi)$ ones from the V-1461 alloy side, both in the HAZ and the BM. The $\delta'(Al_3Li)$ phase had formed in the WM, but the intensity of its reflections decreased in the HAZ from the 1424 alloy side. The intensity of the $S_1(Al_2MgLi)$ metastable phase reflections reduced, i.e., its significant dissolution had occurred. In the WM, the alloying elements, initially presented in the intermetallic phases (in particular, in the $T_1(Al_2CuLi)$ and $S_1(Al_2MgLi)$ ones), were completely or partially dissolved in aluminum. Thus, the extremely non-equilibrium state (the supersaturated solid solution of copper, magnesium, and lithium in aluminum) was resulted by quenching.

Table 10
The EDX analysis results at the BM areas highlighted in Fig. 11.

Spectrum	Al, at.%	Cu, at.%	Mg, at.%	Fe, at.%	Mn, at.%	Zn, at.%	Sc, at.%	Si, at.%	Comments
1	99.25	0.35	0.22		0.06	0.12			*Al grain*
2	94.32	3.80	1.27		0.07	0.34		0.20	*Eutectics*
3	98.36	0.61	1.03						*Al grain*
4	94.76	1.33	2.27	0.13	0.10			1.42	*Eutectics*
5	97.14	0.47	2.29		0.09				*Al grain*
6	91.53	2.91	5.00		0.09				*Eutectics*
7	96.20	0.35	3.35		0.10				*Al grain*
8	95.35	1.82	2.73		0.10				*Eutectics*
9	95.42	0.33	3.93		0.09	0.23			*Al grain*
10	94.32	0.57	4.41	0.27	0.10	0.32			*Eutectics*
11	96.11	0.57	3.10		0.07	0.17			*Al grain*
12	94.67	1.61	3.72						
13	96.26	0.59	3.15						*Al grain*
14	90.15	3.80	5.59		0.33		0.07	0.06	
15	82.63	8.19	8.11	0.16	0.16	0.56		0.19	
16	94.02	3.51	2.09	0.13	0.09			0.16	
17	93.98	2.90	3.06					0.06	
18	97.13	0.85	1.95		0.07				*Al grain*
19	88.92	6.48	3.85			0.48		0.27	
20	97.14	0.83	1.95		0.08				*Al grain*
21	88.21	4.30	6.70	0.18	0.14	0.38		0.09	
22	95.39	0.30	4.31						*Al grain*

Table 11
The cooling rate parameters and the solidification modes.

Alloy	$G \times R = \frac{dT}{dt}$ K/s	$\frac{G}{R}$ K×s/mm^2
1424 (Al-4.9Mg-1.65Li)	1342	0.30
V-1461 (Al-2.7Cu-1.8Li-0.3 Mg)	2570	0.58

The influence of the quenching process essentially depended on the composition of the alloying elements, i.e. the Al-Mg-Li and Al-Cu-Li systems. At room temperature, the most unstable structure in the heat treatable aluminum alloys, characterized by the phase transformations in the solid state, was the supersaturated solid solution of the alloying components in aluminum, the concentration of which could be higher by ten times than the equilibrium levels.

The presence of copper in each of the dissimilar joint zones indicated active mixing of the weld pool. In this case, convective mass transfer played a more important role compared to diffusion. The key convection mechanism was caused by the surface tension gradients on the weld pool due to spatial temperature variations, namely Marangoni convection. This phenomenon promoted different molten metal flows. Marangoni convection depended on the surface tension, which in turn was determined by the temperature range and the chemical composition of the joined alloys.

The shape and the sizes of the WM depended on convective flows of the molten metal in the weld pool due to the surface tension gradient, which was determined by the Marangoni number. The Marangoni number was the ratio of the surface tension force to the molten metal viscosity, and was a measure of the convective flow strength for the molten metal in the weld pool:

$$Ma = -\frac{d\gamma}{dT}\frac{L\Delta T}{\mu\alpha}, \quad (5)$$

where μ was viscosity, α was thermal diffusivity, L was the characteristic length of the weld pool, equal to its width, ΔT was the difference between temperatures inside the weld pool.

It was especially necessary to highlight the negligible effect of quenching on the changes in the intermetallic phases of the Al-Mg-Li system at the 1424 alloy side [15]. After welding and subsequent quenching of the dissimilar joint, only weak reflections of the $S_1(Al_2MgLi)$ phase were observed in the WM, but the $\delta'(Al_3Li)$ one was absent. The absence of such strengthening phases and the slight change in the mechanical properties after PWHT enabled to suggest that the above mechanism of the formation of the Guinier–Preston (GP) zones and the intermediate metastable phases was not observed, since magnesium was not contributed to such processes in the Al-Mg system.

It should be noted that no clear conclusion was found in publications about the formation of the GP zones in the Al-Mg-Li alloys. For example, it was stated in [39] that the GP zones represented a short-range ordering of dissolved copper and magnesium atoms, but it was reported in [40] that the GP zones could not be found in the Al-Mg-Li grades. The research by the authors confirmed this statement, since the 1420 and 1424 alloys (containing no copper) were not quenched. Thus, the role of quenching was reduced to the formation of a homogenized aluminum solid solution supersaturated with the alloying elements. A similar conclusion was drawn in [41].

According to the diffraction patterns obtained with synchrotron radiation in the HAZ at the 1424 (Al-Mg-Li) alloy side (Fig. 13), any reflections of the $\delta'(Al_3Li)$ strengthening phase were not observed, although they were present in the BM (for both joints as-welded and after quenching). In the as-welded HAZ, the intense peaks of the $S_1(Al_2MgLi)$ phase were found, which dissolved upon quenching.

After quenching, the absence of the strengthening phases and the slight change in the mechanical properties enabled to suggest that the mechanism of the formation of the GP zones and the subsequent precipitation of the intermediate metastable phases did not match to the Al-Mg alloy, i.e. magnesium did not form the GP zones. Nevertheless, the $\delta'(Al_3Li)$ phase was found in the WM, which could indicate the influence of copper on its formation in welding due to the presence of the GP zones. In the HAZ at the V-1461 (Al-Cu-Li) alloy side, the GP zones with both $\delta'(Al_3Li)$ and $T_3'(Al_5CuLi_3)$ phases formed upon quenching, improving the mechanical properties of the dissimilar welded joint.

Artificial aging caused the formation of the $\delta'(Al_3Li)$ main strengthening phase over the entire WM volume. At the same time, its content rose according to the reflections in the diffraction patterns. In the BM and the HAZ at the V-1461 alloy side, the $T_1(Al_2CuLi)$ and $\delta'(Al_3Li)$ phases were observed.

The performed studies enabled to assess the phase transformation sequence in laser welding and subsequent PWHT for the investigated alloys and their relationship with the mechanical properties (Fig. 16).

Quenching enabled to form the $\delta'(Al_3Li)$, $T_3'(Al_5CuLi_3)$ strengthening phases in the WM, increasing the ultimate tensile strength of the dissimilar welded joint up to 70 % and elongation up to 95 % of those for the 1424 alloy. Subsequent artificial aging contributed to rising the

contents of the $T_1(Al_2CuLi)$ and δ'(Al_3Li) phases, enhancing the ultimate tensile strength and the yield point up to 80 % and 89 % of those for the 1424 alloy, respectively.

Fig. 17 shows the evolution of the microstructures and the phase transformations, considering the metallurgy processes in the WM that depended on the alloying system, the thermophysical properties, the solidification modes, the convective flows of the molten metal in the weld pool, the rapid local non-equilibrium heating upon melting and subsequent solidification, as well as the optimal PWHT parameters.

For improving the mechanical properties of the 1424/V-1461 dissimilar welded joint, PWHT should include quenching at 530 °C for 30 min and subsequent artificial aging at 175 °C for 16 h. In this case, the following levels were achieved: the ultimate tensile strength of 411 MPa, the yield point of 327 MPa and elongation of 1.7 %, which were close to those for the 1424 alloy, as the weakest one.

5. Conclusions

The evolution of the microstructure and the phase transformations, as well as their influence on the mechanical properties was studied for the dissimilar welded joint of the heat treatable aluminum–lithium alloys of the third generation. Despite the need to find the parameters of heat treatment, it provides the opportunity to optimize the microstructure of such a kind of weld joints. However, the features of the obtained alloying system in the welded material in this case cannot provide the full range of the weakest (1424 in this case) initial alloy's properties. Based on the results, this study concludes the following:

1. Welded material consists of dendritic Al grains with lowered alloying elements content surrounded by Cu-rich eutectics consisting of at least Al, $T_1(Al_2CuLi)$ and $T_3(Al_5CuLi_3)$. Welded material also contains δ′(Al_3Li) and S′(Al_2MgLi) phases. Such a microstructure significantly affected the mechanical performance of the material decreasing ultimate and yield tensile strength and elongation down to 262 MPa, 234 MPa and 0.83 % respectively (51, 63 and 12 % of the properties of 1424 alloy).
2. Quenching at 530 °C for 30 min with subsequent water cooling caused the change in the initial dendritic grain shape to the rounded one and the eutectics dissolution. Subsequent artificial aging at 175 °C for 16 h led to the formation of precipitation of the δ′(Al_3Li), $T_1(Al_2CuLi)$ and $T_3(Al_5CuLi_3)$ phases in the weld material.
3. Heat treatment significantly enhanced the mechanical performance on the welded material. Thus, **quenching** led to a growth of ultimate and yield tensile strength and elongation up to **383 MPa** and **220 MPa** and **6.89 %** respectively (75, 60 and 96 % of the properties of 1424 alloy). **Artificial aging** resulted in the additional increase in ultimate and yield tensile strength up to **411** and **327** MPa (80 and 89 % of 1424 alloy's values) but also in significant drop of elongation down to **1.70** % (24 % of the 1424 alloy's value) which is caused by excessive hardening by the precipitations.

Declaration of Competing Interest

The authors declare that they have no known competing financial interests or personal relationships that could have appeared to influence the work reported in this paper.

Data availability

Data will be made available on request.

Acknowledgements

The research was carried out within the state assignment of Ministry of Science and Higher Education of the Russian Federation. Part of the work was done at the shared research center SSTRC on the basis of the VEPP-4 - VEPP-2000 complex at BINP SB RAS.

References

[1] T. Dursun, C. Soutis, Recent developments in advanced aircraft aluminium alloys, Mater. Des. 56 (2014) 862–871, https://doi.org/10.1016/j.matdes.2013.12.002.
[2] R.J. Rioja, J. Liu, The evolution of Al-Li base products for aerospace and space applications, Metall. Mater. Trans. A 43 (2012) 3325–3337, https://doi.org/10.1007/s11661-012-1155-z.
[3] A. Abd El-Aty, Y. Xu, X. Guo, S.-H. Zhang, Y. Ma, D. Chen, Strengthening mechanisms, deformation behavior, and anisotropic mechanical properties of Al-Li alloys: a review, J. Adv. Res. 10 (2018) 49–67, https://doi.org/10.1016/j.jare.2017.12.004.
[4] T. Dorin, A. Vahid, J. Lamb, Aluminium Lithium Alloys, in: Fundam. Alum. Metall., Elsevier, 2018, pp. 387–438, doi: 10.1016/B978-0-08-102063-0.00011-4.
[5] E.A. Starke, J.T. Staley, Application of modern aluminum alloys to aircraft, Prog. Aerosp. Sci. 32 (1996) 131–172, https://doi.org/10.1016/0376-0421(95)00004-6.
[6] N.E. Prasad, A.A. Gokhale, R.J.H. Wanhill, Aluminum-lithium Alloys, Elsevier, 2014, doi: 10.1016/C2012-0-00394-8.
[7] S.C. Wang, M.J. Starink, Precipitates and intermetallic phases in precipitation hardening Al–Cu–Mg–(Li) based alloys, Int. Mater. Rev. 50 (2005) 193–215, https://doi.org/10.1179/174328005X14357.
[8] J. Enz, M. Kumar, S. Riekehr, V. Ventzke, N. Huber, N. Kashaev, Mechanical properties of laser beam welded similar and dissimilar aluminum alloys, J. Manuf. Process. 29 (2017) 272–280, https://doi.org/10.1016/J.JMAPRO.2017.07.030.
[9] J. Enz, S. Riekehr, V. Ventzke, N. Kashaev, Influence of the local chemical composition on the mechanical properties of laser beam welded Al-Li alloys, Phys. Proc. 39 (2012) 51–58, https://doi.org/10.1016/j.phpro.2012.10.013.
[10] F. Liu, B. Zhou, Y. Mao, C. Huang, Y. Chen, Z. Wang, Microstructure and mechanical properties of laser welded joints between 2198/2060 Al–Li alloys, Mater. Sci. Technol. 34 (2018) 111–122, https://doi.org/10.1080/02670836.2017.1365221.
[11] B. Han, Y. Chen, W. Tao, H. Li, L. Li, Microstructural evolution and interfacial crack corrosion behavior of double-sided laser beam welded 2060/2099 Al-Li alloys T-joints, Mater. Des. 135 (2017) 353–365, https://doi.org/10.1016/j.matdes.2017.09.042.
[12] H. Liu, Z. Lei, H. Jiang, J. Zou, Z. Guo, R. Bai, D. Wang, Study on shear buckling failure of laser-welded dissimilar aluminum alloy (Al-Li-2099/Al-Li-S4) stiffened panel, J. Laser Appl. 34 (2022) 022012, https://doi.org/10.2351/7.0000600.
[13] D. Chen, X. Zhan, T. Liu, Y. Zhao, N. Qi, L. Sun, Effect of porosity morphology and elements characteristics on mechanical property in T-joints during dual laser-beam bilateral synchronous welding of 2060/2099 Al-Li alloys, Opt. Laser Technol. 140 (2021) 107019, https://doi.org/10.1016/J.OPTLASTEC.2021.107019.
[14] A. Malikov, N. Bulina, M. Sharafutdinov, A. Orishich, Study of the structure and phase composition of laser welded joints of Al-Cu-Li alloy under different heat treatment conditions, Int. J. Adv. Manuf. Technol. 104 (2019) 4313–4324, https://doi.org/10.1007/s00170-019-04286-w.
[15] A. Malikov, A. Orishich, N. Bulina, E. Karpov, M. Sharafutdinov, Effect of post heat treatment on the phase composition and strength of laser welded joints of an Al–Mg–Li alloy, Mater. Sci. Eng. A 765 (2019) 138302, https://doi.org/10.1016/j.msea.2019.138302.
[16] A. Malikov, A. Orishich, I. Vitoshkin, N. Bulina, E. Karpov, A. Gutakovskii, S. Batsanov, A. Ancharov, R. Tabakaev, Effect of the structure and the phase composition on the mechanical properties of Al–Cu–Li alloy laser welds, Mater. Sci. Eng. A 809 (2021) 140947, https://doi.org/10.1016/j.msea.2021.140947.
[17] A. Malikov, A. Orishich, I. Vitoshkin, E. Karpov, A. Ancharov, Effect of post-heat treatment on microstructure and mechanical properties of laser welded Al-Cu-Mg alloy, J. Manuf. Process. 64 (2021) 620–632, https://doi.org/10.1016/j.jmapro.2021.02.008.
[18] A.G. Malikov, E.V. Karpov, A.M. Orishich, Effect of temperature on the fracture behaviour of heat-treated Al–Cu–Li alloy laser welds under low-cycle fatigue loading, Fatigue Fract. Eng. Mater. Struct. 43 (2020) 1250–1261, https://doi.org/10.1111/ffe.13218.
[19] J. Cheng, G. Song, X. Zhang, C. Liu, L. Liu, Review of techniques for improvement of softening behavior of age-hardening aluminum alloy welded joints, Materials (Basel) 14 (2021) 5804, https://doi.org/10.3390/ma14195804.
[20] L.B. Khokhlatova, N.I. Kolobnev, M.S. Oglodkov, E.A. Lukina, S.V. Sbitneva, Change in phase composition in relation to aging regimes and alloy V-1461 semifinished product structure, Met. Sci. Heat Treat. 54 (2012) 285–289, https://doi.org/10.1007/s11041-012-9498-z.
[21] E.A. Lukina, A.A. Alekseev, L.B. Khokhlatova, M.S. Oglodkov, Regular features of formation of main hardening phases in alloys 1424 of the Al – Mg – Li – Zn system and V-1461 of the Al – Cu – Li – Zn – Mg system, Met. Sci. Heat Treat. 55 (2014) 466–471, https://doi.org/10.1007/s11041-014-9655-7.
[22] L.B. Khokhlatova, N.I. Kolobnev, M.S. Oglodkov, E.D. Mikhaylov, Aluminum-lithium alloys for aircraft building, Metallurgist 56 (2012) 336–341, https://doi.org/10.1007/s11015-012-9580-1.
[23] I.N. Fridlyander, L.B. Khokhlatova, N.I. Kolobnev, K. Rendiks, G. Tempus, Thermally stable aluminum-lithium alloy 1424 for application in welded fuselage, Met. Sci. Heat Treat. 44 (2002) 3–8, https://doi.org/10.1023/A:1015359900319.
[24] A.G. Malikov, A.M. Orishich, I.E. Vitoshkin, E.V. Karpov, A.I. Ancharov, Laser welding of dissimilar materials based on thermally hardened aluminum alloys, J. Appl. Mech. Tech. Phys. 62 (2021) 842–850, https://doi.org/10.1134/S0021894421050163/FIGURES/4.

[25] A.I. Ancharov, A.Y. Manakov, N.A. Mezentsev, B.P. Tolochko, M.A. Sheromov, V. M. Tsukanov, New station at the 4th beamline of the VEPP-3 storage ring, Nucl. Instruments Methods Phys. Res. Sect. A Accel. Spectrometers, Detect. Assoc. Equip. 470 (2001) 80–83, https://doi.org/10.1016/S0168-9002(01)01029-4.
[26] M. Zinkevich, T. Velikanova, M. Turchanin, Z. Du, M. Materials Science International Team, Al-Cu-Li Ternary Phase Diagram Evaluation · Phase diagrams, crystallographic and thermodynamic data: Datasheet from MSI Eureka in SpringerMaterials, https://materials.springer.com/msi/docs/sm_msi_r_10_015854_02, (n.d.).
[27] G. Ghosh, M. Materials Science International Team, Al-Li-Mg Ternary Phase Diagram Evaluation · Phase diagrams, crystallographic and thermodynamic data: Datasheet from MSI Eureka in SpringerMaterials, https://materials.springer.com/msi/docs/sm_msi_r_10_012175_03, (n.d.).
[28] S. Katayama, Defect formation mechanisms and preventive procedures in laser welding, in: Handb. Laser Weld. Technol., Elsevier, 2013, pp. 332–373, doi: 10.1533/9780857098771.2.332.
[29] N. Kashaev, V. Ventzke, G. Çam, Prospects of laser beam welding and friction stir welding processes for aluminum airframe structural applications, J. Manuf. Process. 36 (2018) 571–600, https://doi.org/10.1016/j.jmapro.2018.10.005.
[30] B. Fotovvati, S.F. Wayne, G. Lewis, E. Asadi, A review on melt-pool characteristics in laser welding of metals, Adv. Mater. Sci. Eng. 2018 (2018) 1–18, https://doi.org/10.1155/2018/4920718.
[31] H. Zhao, T. DebRoy, Macroporosity free aluminum alloy weldments through numerical simulation of keyhole mode laser welding, J. Appl. Phys. 93 (2003) 10089–10096, https://doi.org/10.1063/1.1573732.
[32] A. Malikov, A. Orishich, A. Golyshev, E. Karpov, Manufacturing of high-strength laser welded joints of an industrial aluminum alloy of system Al-Cu-Li by means of post heat treatment, J. Manuf. Process. 41 (2019), https://doi.org/10.1016/j.jmapro.2019.03.037.
[33] Y.N. Hu, S.C. Wu, L. Chen, Review on failure behaviors of fusion welded high-strength Al alloys due to fine equiaxed zone, Eng. Fract. Mech. 208 (2019) 45–71, https://doi.org/10.1016/J.ENGFRACMECH.2019.01.013.
[34] J. Bi, Z. Liu, J. Chi, H. Wang, C. Tan, X. Jia, Z. Yang, M.D. Starostenkov, G. Dong, Formation mechanisms and control strategies of FQZ softening in Al-Li alloy welded joint, J. Mater. Res. Technol. (2023), https://doi.org/10.1016/j.jmrt.2023.01.147.
[35] A. Yamamoto, H. Tsubakino, R. Nozato, Resistivity study of aging in Al–Li–Cu alloys, Mater. Trans. 36 (1995) 1447–1454, https://doi.org/10.2320/matertrans1989.36.1447.
[36] O.A. Setuykov, I.N. Fridliander, V.F. Shamray, Research of super lattice structure parameters in alloys of Al-Li-Mg system, Mater. Sci. Forum 519–521 (2006) 1907–1912, https://doi.org/10.4028/www.scientific.net/msf.519-521.1907.
[37] S. Wang, L. Zhao, Y. Jin, Influence of post-weld heat treatment on microstructure and mechanical properties of laser beam welded 2195 Al–Li alloy, Mater. Res. Express 6 (2019) 076567, https://doi.org/10.1088/2053-1591/ab1736.
[38] C. Hagenlocher, F. Fetzer, D. Weller, R. Weber, T. Graf, Explicit analytical expressions for the influence of welding parameters on the grain structure of laser beam welds in aluminium alloys, Mater. Des. 174 (2019) 107791, https://doi.org/10.1016/j.matdes.2019.107791.
[39] M. Gäumann, S. Henry, F. Cléton, J.-D. Wagnière, W. Kurz, Epitaxial laser metal forming: analysis of microstructure formation, Mater. Sci. Eng. A 271 (1999) 232–241, https://doi.org/10.1016/S0921-5093(99)00202-6.
[40] J.P. Oliveira, T.G. Santos, R.M. Miranda, Revisiting fundamental welding concepts to improve additive manufacturing: from theory to practice, Prog. Mater Sci. 107 (2020) 100590, https://doi.org/10.1016/J.PMATSCI.2019.100590.
[41] C. Böhm, C. Hagenlocher, J. Wagner, T. Graf, S. Weihe, Analytical description of the criterion for the columnar-to-equiaxed transition during laser beam welding of aluminum alloys, Metall. Mater. Trans. A 52 (2021) 2720–2731, https://doi.org/10.1007/S11661-021-06238-0/FIGURES/8.